

Numerical aspects of Casimir energy computation in acoustic scattering

Timo Betcke^a, Alexander Strohmaier^b, Xiaoshu Sun^{a,*}

^a*Department of Mathematics, University College London, London, WC1E 6BT, UK*

^b*School of Mathematics, University of Leeds, Leeds, LS2 9JT, UK*

Abstract

Computing the Casimir force and energy between objects is a classical problem of quantum theory going back to the 1940s. Several different approaches have been developed in the literature often based on different physical principles. Most notably a representation of the Casimir energy in terms of determinants of boundary layer operators makes it accessible to a numerical approach. In this paper, we first give an overview of the various methods and what is known rigorously about the connection between them. We then present a new numerical scheme for the computation of the Casimir energy for large scale problems, which is based on the spectral properties of the block matrices for the boundary layer operators. This method allows for Casimir energy calculation for large-scale practical problems and significantly speeds up the computations in that case. We also discuss the connection to the Krein-spectral shift function and computational aspects.

Keywords: Krein spectral shift function, Casimir energy, Krylov subspace, inverse-free generalized eigenvalue problem, Bempp-cl

1. Introduction

Casimir interactions are forces between objects such as perfect conductors. Hendrik Casimir predicted and computed this effect in the special case of two planar conductors in 1948 using a divergent formula for the zero point energy and applying regularisation to it [1]. This resulted in the famous formula for the attractive Casimir force per unit area

$$F(a) = -\frac{1}{A} \frac{\partial \mathcal{E}}{\partial a} = -\frac{\hbar c \pi^2}{240 a^4},$$

between two perfectly conducting plates, where A is the cross-sectional area of the boundary plates and \mathcal{E} is the Casimir energy as computed from a zeta regularised mode sum. The result here is for the electromagnetic field which differs by a factor of two from the force resulting from a massless scalar field. This force was measured experimentally by Sparnaay about 10 years later [2] and the Casimir effect has since become famous for its intriguing derivation and its counterintuitive nature. In 1996, precision measurements of the Casimir force between the extended bodies were conducted by S.K. Lamoreaux [3] confirming the theoretical predictions including the corrections for realistic materials. From 2000 to 2008, the Casimir force has been measured in various experimental configurations, such as cylinder-cylinder [4], plate-plate [5], sphere-plate [6] and sphere-comb [7]. The presence of the Casimir force has also been quoted as evidence for the zero point energy of the vacuum having direct physical significance. The classical way to compute Casimir forces mimicks Casimir's original computation and is based on zeta function regularisation of the vacuum energy. This has been carried out for a number of particular geometric situations (see [8, 9, 10, 11, 12] and references therein). The derivations

*Corresponding author

URL: t.betcke@ucl.ac.uk (Timo Betcke), a.strohmaier@leeds.ac.uk (Alexander Strohmaier), xiaoshu.sun.18@ucl.ac.uk (Xiaoshu Sun)

are usually based on special functions and their properties and require explicit knowledge of the spectrum of the Laplace operator.

In 1960s, Lifshitz and collaborators extended and modified this theory to the case of dielectric media [13] gave derivations based on the stress energy tensor. It has also been realised by quantum field theorists (see e.g. [14, 13, 15, 16, 17]) with various degrees of mathematical rigour that the stress energy approach yields Casimir's formula directly without the need for renormalisation or artificial regularisation. This tensor is defined by comparing the induced vacuum states of the quantum field with boundary conditions and the free theory. Once the renormalised stress energy tensor is mathematically defined, the computation of the Casimir energy density becomes a problem of spectral geometry (see e.g. [18]). The renormalised stress energy tensor and its relation to the Casimir effect can be understood at the level of rigour of axiomatic algebraic quantum field theory. We note however that the computation of the local energy density is non-local and requires some knowledge of the spectral resolution of the Laplace operator, the corresponding problem of numerical analysis is therefore extremely hard.

Lifshitz and collaborators also offered an alternative description based on the van der Waals forces between molecules. The plates consist of a collection of atomic-scale electric dipoles randomly oriented in the absence of the external forcing field. Quantum and thermal fluctuations may make the dipoles align spontaneously, resulting in a net electric dipole moment. The dipoles in the opposite plate feel this field across the gap and align as well. The two net electric dipole moments make the two plates attract each other. This approach emphasizes the influence from the materials more than the fluctuations in the empty space between the plates.

Somewhat independently from the spectral approach determinant formulae based on the van der Waal's mechanism were derived by various authors. We note here Renne [19] who gives a determinant formula for the van der Waals force based on microscopic considerations. Various other authors give path-integral considerations based on considerations of surface current fluctuations [20, 21, 22, 23, 24, 25, 26, 27, 28]. The final formulae proved suitable for numerical schemes and were also very useful to obtain asymptotic formulae for Casimir forces for large and small separations. The mathematical relation between the various approaches remained unclear, with proofs of equality only available in special cases. A full mathematical justification of the determinant formulae as the trace of an operator describing the Casimir energy was only recently achieved in [29] for the scalar field and [30] for the electromagnetic field. It was also proved recently in [31] that the formulae arising from Zeta regularisation, from the stress energy tensor, and from the determinant of the single layer operator all give the same Casimir forces.

We will now describe the precise mathematical setting and review the theory. Let $\Omega \subset \mathbb{R}^d$ be a non-empty bounded open subset with Lipschitz boundary $\partial\Omega$, which is the union of connected open sets Ω_j , for $j = 1, \dots, N$. We assume that the complement $\mathbb{R}^d \setminus \Omega$ of Ω is connected and the closures of Ω_j are pairwise non-intersecting. We denote the N connected components of the boundary $\partial\Omega$ by $\partial\Omega_j$. We will think of the open set Ω as a collection of objects Ω_j placed in \mathbb{R}^d and will refer to them as *obstacles*.

Then, several unbounded self-adjoint operators densely defined in $L^2(\mathbb{R}^d)$ can be defined.

- The operator Δ is the Laplace operator with Dirichlet boundary conditions on $\partial\Omega$.
- For $j = 1, \dots, N$, the operator Δ_j is the Laplace operator with Dirichlet boundary conditions on $\partial\Omega_j$.
- The operator Δ_0 is the ‘free’ Laplace operator on \mathbb{R}^d with domain $H^2(\mathbb{R}^d)$.

These operators contain the dense set $C_0^\infty(\mathbb{R}^d \setminus \partial\Omega)$ in their domains. If $f : \mathbb{R} \rightarrow \mathbb{R}$ is a polynomially bounded function this set is also contained in the domain of the operators $f(\Delta^{\frac{1}{2}})$, $f(\Delta_j^{\frac{1}{2}})$, and $f(\Delta_0^{\frac{1}{2}})$, in particular the

operator

$$D_f = f(\Delta^{\frac{1}{2}}) - f(\Delta_0^{\frac{1}{2}}) - \left(\sum_{j=1}^N [f(\Delta_j^{\frac{1}{2}}) - f(\Delta_0^{\frac{1}{2}})] \right)$$

is densely defined. It was shown in [29] that under additional analyticity assumptions on f the operator D_f is bounded and extends by continuity to a trace-class operator on $L^2(\mathbb{R}^d)$. These analyticity assumptions are in particular satisfied by $f(\lambda) = (\lambda^2 + m^2)^{\frac{s}{2}}$ for any $s > 0, m \geq 0$ and one has

$$\text{Tr}(D_f) = \frac{s}{\pi} \sin\left(\frac{\pi}{2}s\right) \int_m^\infty \lambda(\lambda^2 + m^2)^{\frac{s}{2}-1} \Xi(i\lambda) d\lambda, \quad (1)$$

where the function Ξ is given by

$$\Xi(\lambda) = \log \det V_\lambda \tilde{V}_\lambda^{-1}$$

and the operators V_k and \tilde{V}_k are certain boundary layer operators that will be defined later. It was proved in [29] that this $V_\lambda \tilde{V}_\lambda^{-1} - 1$ near the positive imaginary axis is indeed a holomorphic family of trace-class operators on the Sobolev space $H^{\frac{1}{2}}(\partial\Omega)$ so that the above determinant is well-defined in the sense of Fredholm. We remark here that the paper [29] assumed the boundary to be smooth and the operators $V_\lambda \tilde{V}_\lambda^{-1}$ was considered as a map on $L^2(\partial\Omega)$. The main result of the paper also holds for Lipschitz boundaries if $L^2(\partial\Omega)$ is replaced by $H^{\frac{1}{2}}(\partial\Omega)$. This requires minor modifications of the proof but we will not discuss this further here, as we are now focusing on computational aspects.

We also recall that by the Birman-Krein formula we have for any even function $h \in \mathcal{S}(\mathbb{R})$ the equality

$$\text{Tr}\left(h(\Delta^{\frac{1}{2}}) - h(\Delta_0^{\frac{1}{2}}) - \left(\sum_{j=1}^N [h(\Delta_j^{\frac{1}{2}}) - h(\Delta_0^{\frac{1}{2}})]\right)\right) = \int_0^\infty h'(\lambda) \xi(\lambda) d\lambda, \quad (2)$$

where

$$\xi(\lambda) = \frac{1}{2\pi i} \log \left(\frac{\det(S(\lambda))}{\det(S_{1,\lambda}) \cdots \det(S_{N,k}(\lambda))} \right)$$

will be called the relative Krein spectral shift function. Here, $S_{j,k}$ are the scattering matrices of Δ_j associated to the objects Ω_j . Note here that the class of functions for which this is true can be relaxed to a certain extent, but even the most general version does not allow unbounded functions such as $f(\lambda)$ with $s > 0, m \geq 0$. The relative spectral shift function can however be related via a Laplace transform to the Fourier transform of the relative spectral shift function (see [32]). Under mild convexity assumptions this can be connected to the Duistermaat-Guillemin trace formula in obstacle scattering theory to give an asymptotic expansion of $\Xi(\lambda)$ in terms of the minimal distance $\delta > 0$ between the obstacles and the linearised Poincaré map of the bouncing ball orbits between the obstacles of that length. One has

$$\Xi(\lambda) = - \sum_j \frac{1}{|\det(I - P_{\gamma_j})|^{\frac{1}{2}}} e^{2i\delta\lambda} + o(e^{-2\delta\text{Im}\lambda}),$$

where the sum is over bouncing ball modes of length 2δ and P_{γ_j} is the associated Poincaré map, where γ_j is the shortest bouncing ball orbits.

The Casimir energy of the configuration Ω for a massless scalar field would then be given by D_f in the case when $f(\lambda) = \lambda$ and is therefore equal to

$$\mathcal{E} = -\frac{\hbar c}{2\pi} \int_0^\infty \Xi(i\lambda) d\lambda.$$

In this paper, we are going to introduce the numerical framework of computing the Casimir energy based on the evaluation of the log determinant of the integral operators in the acoustic case ¹ in Section 2. Afterwards,

¹The mathematical theories and numerical experiments in the Maxwell case have been done as well and they will be reported in another paper.

two efficient methods for computing the integrand of the Casimir energy will be illustrated in Section 3 which makes us compute the large-scale problem efficiently. In Section 4, several examples on computing the Casimir energy between the compact objects will be shown and we will also compare our results with others computed in other methods. Note that all the tests and examples in this paper were computed with version 0.2.4 of the Bempp-cl library [33]. Finally, Section 5 will conclude our paper and discuss the future plan as well.

2. Numerical methods for computing the Casimir energy in acoustic scattering

In this section, we give details of computing the Casimir energy via boundary integral operator discretisations. Assume $\Omega^- \in \mathbb{R}^d$, for $d \geq 2$ is the interior bounded Lebesgue-measurable domain that the scatterer occupies with piecewise smooth Lipschitz boundary Γ . The exterior domain is denoted as $\Omega^+ = \mathbb{R}^d \setminus \overline{\Omega^-}$. \mathbf{n} is the exterior unit normal to the surface Γ pointing outwards from Ω^- and \mathbf{n}_x is normal to Γ at the point $x \in \Gamma$.

In the scalar case, the Casimir energy can be expressed in terms of certain single-layer boundary operator, which we will define below. We then present its relationship with the Krein-Spectral shift function and demonstrate how it can practically be computed.

2.1. The single-layer boundary operator

For the bounded interior domain Ω^- or the unbounded exterior domain Ω^+ , the space of the (locally) square integrable functions is

$$L^2(\Omega^\pm) := \left\{ f : \Omega^\pm \rightarrow \mathbb{C}, f \text{ is Lebesgue measurable and } \int_{\Omega^\pm} |f|^2 < \infty \right\},$$

$$L_{\text{loc}}^2(\Omega^+) := \left\{ f : \Omega^+ \rightarrow \mathbb{C}, f \text{ is Lebesgue measurable and } \int_K |f|^2 < \infty, \text{ for all compact } K \subset \Omega^+ \right\}$$

and note that the subscript ‘‘loc’’ can be removed if the domain is bounded (i.e. $L_{\text{loc}}^2(\Omega^-) = L^2(\Omega^-)$). We define the (local) Sobolev space $H_{\text{loc}}^s(\Omega^\pm)$ as

$$H_{\text{loc}}^s(\Omega^\pm) := \left\{ f \in L_{\text{loc}}^2(\Omega^\pm), \forall \alpha \text{ s.t. } |\alpha| \leq s, D^\alpha f \in L_{\text{loc}}^2(\Omega^\pm) \right\},$$

where $\alpha = (\alpha_1, \alpha_2, \dots, \alpha_d)$ is a multi-index and $|\alpha| = \alpha_1 + \alpha_2 + \dots + \alpha_d$, and the derivative is defined in the weak sense.

For any function $f \in H_{\text{loc}}^1(\Omega)$ we can define the trace γ_D^\pm as

$$\gamma_D^\pm p(x) := \lim_{\Omega^\pm \ni x' \rightarrow x \in \Gamma} p(x').$$

We call the range of the trace operator $H^{1/2}(\Gamma)$. This space can be more rigorously defined. But for the purposes of this paper the description of $H^{1/2}(\Gamma)$ is range space of the trace operator is sufficient. We furthermore need the space $H^{-1/2}(\Gamma)$, which is the dual space of $H^{1/2}(\Gamma)$ with $L^2(\Gamma)$ as pivot space.

We can now define the single-layer boundary $V_k : H^{-1/2}(\Gamma) \rightarrow H^{1/2}(\Gamma)$ as

$$(V_k \mu)(x) := \int_\Gamma g_k(x, y) \psi(y) dS_y, \quad \text{for } \mu \in H^{-1/2}(\Gamma) \text{ and } x \in \Gamma.$$

Here,

$$g_k(x, y) = \begin{cases} \frac{i}{4} H_0^{(1)}(k|x - y|), & \text{for } d = 2 \\ \frac{e^{ik|x-y|}}{4\pi|x-y|}, & \text{for } d = 3, \end{cases} \quad (3)$$

with $H_0^{(1)}$ a Hankel function of the first kind.

2.2. Relation between the Krein spectral shift function and the single-layer boundary operator

By [29], the Krein spectral shift function is defined as

$$\xi(k) = \frac{1}{2\pi i} \log \left(\frac{\det(S(k))}{\det(S_{1,k}) \cdots \det(S_{N,k})} \right),$$

where $S_{i,n}$ is the scattering matrix associated with the n th scatterer. These scattering matrices can be constructed $S_{i,n} = I + 2T_{i,n}$, where I is the identity matrix and $T_{i,n}$ is the T -matrix. The method of computing the T -matrix is fully discussed in [34] and [35].

The following theorem links the single-layer boundary operator with the Krein spectral shift function.

Theorem 1. [29] Consider Ω as a domain assembling from individual objects Ω_i . Let V_k be the single-layer boundary operator defined on the boundary $\partial\Omega = \bigcup_{i=1}^N \partial\Omega_i$, and \tilde{V}_k is the “diagonal part” of V_k by restricting the integral kernel to the subset $\bigcup_{i=1}^N \partial\Omega_i \times \partial\Omega_i \subset \partial\Omega \times \partial\Omega$ then the operator $V_k \tilde{V}_k^{-1}$ is trace-class and

$$\Xi(k) = \log \det(V_k \tilde{V}_k^{-1}).$$

Then for $k > 0$, we have

$$-\frac{1}{\pi} \text{Im}\Xi(k) = \frac{i}{2\pi} (\Xi(k) - \Xi(-k)) = \xi(k)$$

and by taking $m = 0$ and $s = 1$ in (1), this gives the formula

$$\text{Tr} \left(\Delta^{\frac{1}{2}} + (N-1)\Delta_0^{\frac{1}{2}} - \sum_{i=1}^N \Delta_j^{\frac{1}{2}} \right) = \frac{1}{\pi} \int_0^\infty \Xi(ik) dk. \quad (4)$$

Equation (4) is used to compute the Casimir energy between the objects and the formula is written as

$$\mathcal{E} = -\frac{\hbar c}{2\pi} \int_0^\infty \Xi(ik) dk. \quad (5)$$

2.3. Galerkin discretization and boundary element spaces

In order to compute the integral (5), we need to compute the log determinant of the operators $V_k \tilde{V}_k^{-1}$. In this section we discuss Galerkin discretisations to compute this quantity.

Define the triangulation \mathcal{T}_h of the boundary surface Γ with triangular surface elements τ_l and associated nodes \mathbf{x}_i s.t. $\overline{\mathcal{T}_h} = \bigcup_l \overline{\tau_l}$, where h is the mesh size and define the space of the continuous piecewise linear functions

$$P_h^1(\Gamma) = \{v_h \in C^0(\Gamma) : v_h|_{\tau_l} \in \mathbb{P}_1(\tau_l), \text{ for } \tau_l \in \mathcal{T}_h\},$$

where $\mathbb{P}_1(\tau_l)$ denotes the space of polynomials of order less than or equal to 1 on τ_ℓ . We have

$$P_h^1(\Gamma) := \text{span}\{\phi_j\} \subset H^{-\frac{1}{2}}(\Gamma)$$

with

$$\phi_j(\mathbf{x}_i) = \begin{cases} 1, & i = j, \\ 0, & i \neq j \end{cases}$$

being the nodal basis functions.

Remark 1. Since $H^{-1/2}(\Gamma)$ does not require continuity we could use a space of simple piecewise constant functions. The reason why we choose piecewise linear functions is the size of the arising matrix systems for dense calculations. The computation of the log-determinant requires $\mathcal{O}(n^3)$ operations, where n is the dimension of our approximation basis. For sphere-like and other similar geometries there are in practice roughly twice as many triangles as nodes in the mesh. Hence, while the assembly cost with piecewise linear functions is higher, the resulting matrix has only half the dimension, resulting in roughly a factor eight reduction of computational complexity for the log determinant. A disadvantage is that on geometries with corners or edges the converges close to these singularities is suboptimal with continuous piecewise linear functions.

Having defined the basis function ϕ_j , we can represent each element inside the Galerkin discretization form. Assume there are N objects, then the matrix of the operator V_k is an N by N block matrix, written as

$$V(k) = \begin{bmatrix} V_{11}(k) & V_{12}(k) & \cdots & V_{1N}(k) \\ V_{21}(k) & V_{22}(k) & \cdots & V_{2N}(k) \\ \vdots & \vdots & \ddots & \vdots \\ V_{N1}(k) & V_{N2}(k) & \cdots & V_{NN}(k) \end{bmatrix} \quad (6)$$

and the matrix \tilde{V}_k is the diagonal part of V_k :

$$\tilde{V}(k) = \begin{bmatrix} V_{11}(k) & 0 & \cdots & 0 \\ 0 & V_{22}(k) & \cdots & 0 \\ \vdots & \vdots & \ddots & \vdots \\ 0 & 0 & \cdots & V_{NN}(k) \end{bmatrix}. \quad (7)$$

Therefore, the element in the m th row and n th column of the block matrix $V_{ij}(k)$ is

$$V_{ij}^{(m,n)}(k) = \langle V_{ij}(k)\phi_m^{(i)}, \phi_n^{(j)} \rangle = \int_{\Gamma_j} \overline{\phi_n^{(j)}(\mathbf{x})} \int_{\Gamma_i} g_k(\mathbf{x}, \mathbf{y}) \phi_m^{(i)}(\mathbf{y}) dS_{\mathbf{y}} dS_{\mathbf{x}}, \quad (8)$$

where $\boldsymbol{\phi}^{(i)} = [\phi_1^{(i)} \quad \phi_2^{(i)} \quad \dots \quad \phi_N^{(i)}]$ is the set of basis functions defined on the i th object and

$$\langle f, g \rangle = \int_{\Gamma} f(\mathbf{x}) \overline{g(\mathbf{x})} dS_{\mathbf{x}}$$

denotes the standard $L^2(\Gamma)$ inner product.

The value of $\Xi(ik) = \log \det(V(ik)\tilde{V}(ik)^{-1})$ can now be explicitly computed by evaluating the corresponding log determinants.

The function $\Xi(ik)$ has a very favourable decay behaviour for growing k that we can use to limit the number of quadrature points necessary to evaluate the corresponding Casimir integral, namely under certain convexity assumptions on the obstacles it holds that

$$\Xi(ik) = \mathcal{O}(e^{-2Zk}).$$

Here, Z is the minimum distance between the obstacles [36, Theorem 4.1].

This result can be justified heuristically, using a simple matrix perturbation argument. Consider a symmetric matrix A partitioned as

$$A = \begin{bmatrix} A_1 & 0 \\ 0 & A_2 \end{bmatrix}.$$

and a symmetric matrix E partitioned as

$$E = \begin{bmatrix} 0 & E_1^T \\ E_1 & 0 \end{bmatrix}$$

Then it holds for the i th eigenvalue $\lambda_i(A)$ and the i th eigenvalue $\lambda_i(A + E)$ that

$$|\lambda_i(A) - \lambda_i(A + E)| \leq \frac{\|E\|^2}{\text{gap}_i},$$

where gap_i is the distance of $\lambda_i(A)$ to the spectrum of A_2 if $\lambda_i(A)$ is an eigenvalue of A_1 , and to the spectrum of A_1 if $\lambda_i(A)$ is an eigenvalue of A_2 . Details can be found in [37].

Now assume that we have two different obstacles. Then we have $A_1 = V_{11}(k)$, $A_2 = V_{22}(k)$ and $E_1 = V_{21}$ as the matrix of cross interactions between the two obstacles. The Green's function between two obstacles decays exponentially like e^{-Zk} , where Z is the minimal distance between them, resulting in a matrix perturbation result of the form $|\lambda_i(V) - \lambda_i(\tilde{V})| = O(e^{-2Zk})$ for increasing k , from which the corresponding perturbation result for the log determinant follows.

This purely linear algebraic consideration is not fully robust as it ignores the importance of the eigenvalue gap in the perturbation result. But we can heuristically explain the gap as follows. On the continuous level the perturbations E_1 and E_2 are compact, so the tail end of the spectrum that converges to zero with small values of gap_i , is little effected by E , and the corresponding eigenvalues have a contribution of $\log \left| \frac{\lambda_i(A)}{\lambda_i(A+E)} \right| \approx 0$ to the value of Ξ . The relevant eigenvalues are the larger ones who for distinct obstacles have a sufficiently large value of gap_i .

While the linear algebra argument is useful to give a heuristical explanation, it is not as rigorous as the analytical result in [36]. In particular, we want to emphasize that the exponential decay bound with the quadratic factor also holds if the two obstacles are identical, which is not obvious from pure linear algebraic considerations. An example of this is given in Figure 1.

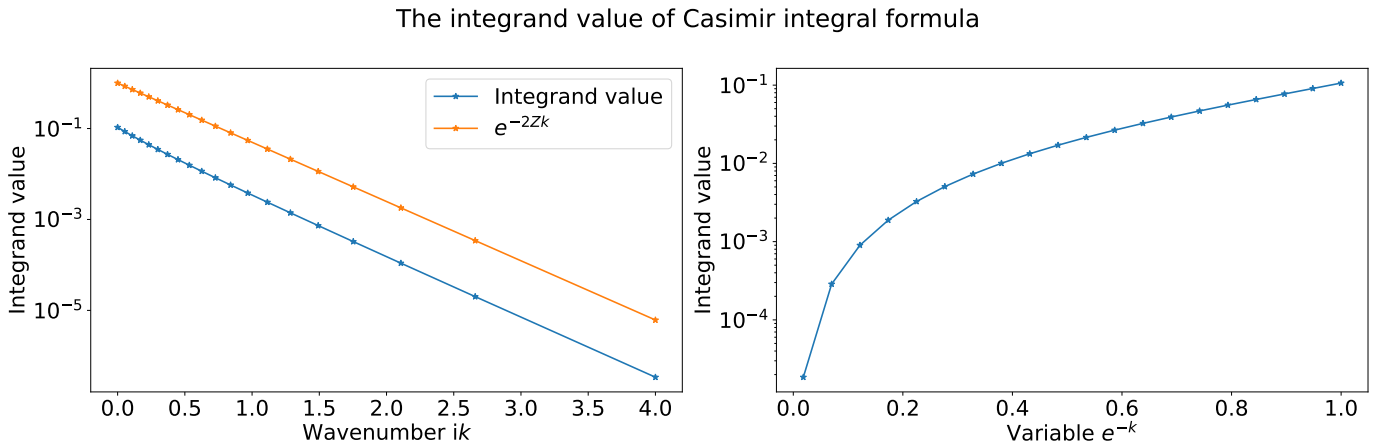


Figure 1: (Left) Exponential decay of $\Xi(ik)$ for two identical spheres with radius $R = 1$ and minimum distance $Z = 1.5$. The red line is the decay bound and the blue line is the actual decay. (Right). The integrand $\Xi(ik)$ after variable transformation to apply a numerical trapezoid rule for its evaluation.

This nice numerical property for the integrand $\Xi(ik)$ simplifies the numerical integration. One can apply the normal trapezoidal rule to calculate the integral $\int_0^\infty \Xi(ik) dk = \int_0^\infty \log \frac{\det V(ik)}{\det \tilde{V}(ik)} dk$ with k changed to y with $y = e^{-k}$. Figure 1 (Right) plots the integrand with regard to the new variable y .

3. Efficient methods for computing $\log \det(V(ik)\tilde{V}(ik)^{-1})$

By Section 2, to compute the Casimir energy, it is necessary to evaluate the term $\log \det(V(ik)\tilde{V}(ik)^{-1})$ with different values of k . In this section, several efficient methods will be introduced to compute this log determinant.

The log determinant of the matrix $V(ik)\tilde{V}(ik)^{-1}$ is equal to the sum of the logarithm of the eigenvalues of $V(ik)\tilde{V}(ik)^{-1}$. Since $\tilde{V}(ik)$ is a compact perturbation of $V(ik)$, most of the eigenvalues of the matrix $V(ik)\tilde{V}(ik)^{-1}$ are close to 1 (shown in Figure 2) and contribute little to the value of the Casimir energy. Hence, we do not need to compute all eigenvalues but only the extremal ones, making subspace methods such as Krylov solvers attractive for this problem.

In what follows we demonstrate and compare iterative solver approaches based on the inverse free Krylov subspace method [38] [39], and based on standard Arnoldi iterations [40]. We will also discuss on acceleration strategy which is based on the idea of recycling projection bases from one quadrature point to the next.

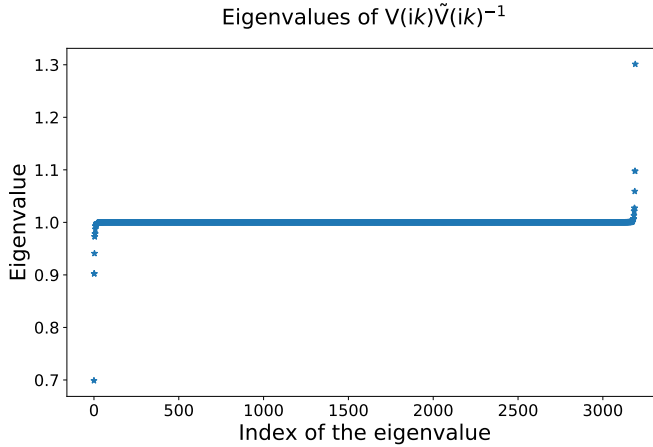


Figure 2: The eigenvalues of the matrix $V(ik)\tilde{V}(ik)^{-1}$ when $ik = 0.8i$. The scatterers are two spheres with equal radii $r_1 = r_2 = 1$ and the minimal distance between them is $Z = 0.5$. The grid size of the mesh is $h = 0.1$.

3.1. Method I: Inverse-free Krylov subspace method

Consider the eigenvalue problem:

$$V(ik)\tilde{V}(ik)^{-1}\mathbf{x} = \lambda\mathbf{x}, \quad (9)$$

where λ is the eigenvalue and \mathbf{x} is the corresponding eigenvalue. This eigenvalue problem is equivalent to the following generalized eigenvalue problem:

$$V(ik)\tilde{\mathbf{x}} = \lambda\tilde{V}(ik)\tilde{\mathbf{x}}. \quad (10)$$

An important property of this problem is that as we are only interested in ik along the imaginary axis, the corresponding matrix $\tilde{V}(ik)$ is positive definite in the scalar case, and $V(ik)$ is still symmetric.

In [38][39], the authors proposed an inverse-free Krylov subspace method for computing a few extreme eigenvalues of the symmetric definite generalized eigenvalue problem. The following algorithms summarizes the method.

Algorithm 1: Inverse-free Krylov subspace method for computing multiple extreme eigenvalues of the generalized eigenvalue problem $A\mathbf{x} = \lambda B\mathbf{x}$

Input: Symmetric matrix $A \in \mathbb{R}^{n \times n}$, s.p.d matrix $B \in \mathbb{R}^{n \times n}$, an initial approximation \mathbf{x} with $\|\mathbf{x}\| = 1$, a given shift ρ and the dimension of the Krylov subspace $m \geq 1$

Output: A set of approximate eigenvalues of $A\mathbf{x} = \lambda B\mathbf{x}$ and associated eigenvectors.

- 1: Construct a basis Z_m for the Krylov subspace $K_m = \text{span}(\mathbf{x}, (A - \rho B)\mathbf{x}, \dots, (A - \rho B)^{m-1}\mathbf{x})$ with dimension m
 - 2: Project A and B on Z : $A_m = Z_m^T(A - \rho B)Z_m$, $B_m = Z_m^TBZ_m$
 - 3: Compute all the eigenpairs $\{(\tilde{\lambda}_i, \mathbf{x}_i)\}_{i=1,\dots,m}$ for the matrix pencil (A_m, B_m)
 - 4: Reverse the shift to obtain $\lambda_i = \tilde{\lambda}_i + \rho$.
-

Why do you say extreme? Isn't the algorithm finding eigenvalues close to the shift? Algorithm 1 approximates m eigenvalues close to the shift ρ for the matrix pencil (A, B) , where m is the dimension of the Krylov subspace K_m in Step 1, Algorithm 1. The question is what shift strategy to use for ρ . In numerical experiments it turned out that for the KSSF problem choosing $\rho = 1$ sufficiently approximate the eigenvalues that have the main contribution to $\log \det(V(ik_j)\tilde{V}(ik_j)^{-1})$.

The main cost of the inverse free Krylov subspace method is the computation of the Krylov subspace and the projection of the matrices A and B . In our case these are large dense matrices representing integral operators. In order to reduce the cost of computing a Krylov subspace basis for each wavenumber ik we can use a recycling strategy based on the idea that a Krylov subspace for a previous quadrature point in the KSSF integral will be a good approximation to a Krylov subspace for the current quadrature point. We initially compute a Krylov basis for the wavenumber ik_1 associated with the first quadrature point. We then extract several eigenvectors associated with the extremal eigenvalues based on Algorithm 1 and then orthogonalize to obtain an initial approximation basis for the wavenumber ik_2 . For this wavenumber we project the matrices onto the recycled basis, compute approximate eigenpairs $(\tilde{\lambda}_i, \tilde{x}_i)$ and then extend the subspace basis with the residuals $r_i = V(ik)\tilde{x}_i - \tilde{\lambda}_i\tilde{V}(ik)\tilde{x}_i$. With the extended subspace we recompute the eigenpairs for the second wavenumber's case and extract eigenvectors as starting basis for the third wavenumber, and so on.

3.2. Method II: Standard Arnoldi method

An alternative to the inverse-free projection method is to use standard Arnoldi to construct the Krylov subspace $K_m(V(ik)\tilde{V}(ik)^{-1}, b)$, where b is some initial vector and m is the dimension of this Krylov subspace, and to then compute the eigenvalues of the resulting projected Hessenberg matrix H_m (see [41]).

The computation of $\tilde{V}(ik)^{-1}y$ for some vector y can be efficiently implemented since $\tilde{V}(ik)$ is simply a block-diagonal matrix with the discretised single-layer potentials for each domain as block matrices. Hence, we just need to compute LU decompositions of these operators, and not of the whole system matrix. Similarly to the inverse free method we can again use a recycling approach based on the same idea of expanding our subspace with computed residuals, but now projecting $V(ik)\tilde{V}(ik)^{-1}$ onto the recycled space.

3.3. Comparison between inverse-free Krylov subspace and standard Arnoldi method with or without recycling subspaces

In this section we compare the standard Arnoldi, inverse free subspace method, and their recycled variants. The example is two spheres with equal radii $r_1 = r_2 = 1$. Again, the minimum distance between them is denoted by Z , which is set as 0.5, 1.5 and 3.0.

The dimension of the Krylov subspace m in Algorithm 1 and Arnoldi iterations is $m = 100$. The number of the recycled eigenvectors is not fixed but depends on the number of the relevant eigenvalues in each wavenumber case. In our experiments, we only recycle the eigenvector whose corresponding eigenvalue has the logarithm greater than 10^{-s} , where $s = 3, 4, 5$ when $Z = 0.5, 1.5, 3.0$, respectively. In this case, the number of the recycled eigenvectors becomes less and less as the k gets larger. Figure 3 plots the dimension of the extended subspace for each wavenumber case. It is equal to the number of the recycled eigenvectors plus the number of the residuals $\{r_i\}_i$.

I do not understand how many vectors you keep in the recycling strategy. Do you always limit to 100 or do you have more? The number anyway seems excessive given that the problem overall is not too large (dimension something around 2 or 3k?)

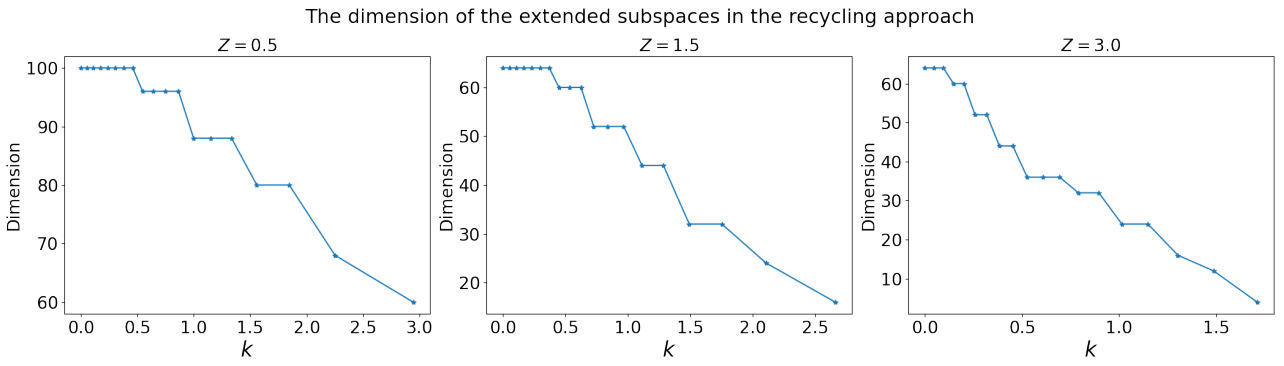


Figure 3: The dimension of the extended subspaces in the recycled approach for each wavenumber case, which is equal to the number of the recycled eigenvectors plus the number of the residuals $\{\mathbf{r}_i\}_i$. The recycled eigenvector has the corresponding eigenvalue whose logarithm is larger than 10^{-s} , where $s = 3, 4, 5$ when $Z = 0.5, 1.5, 3.0$, respectively. The scatterers are two spheres with equal radii $R = 1$ with distance $Z = 0.5, 1.5$ and 3.0 .

Table 1 lists the relative error for approximating the value of $\log \det(\mathbf{V}(ik)\tilde{\mathbf{V}}(ik)^{-1})$ computed via the inverse-free Krylov subspace method and standard Arnoldi method with or without recycling the subspace. [The reference value is computed by the direct dense computation of the log determinant](#). It indicates that with the settings above, one can have at least three significant digits accuracy.

Distance Z	Wavenumber k	Inverse-free (no recycling)	Inverse-free (recycling)	Standard Arnoldi (no recycling)	Standard Arnoldi (recycling)
$Z = 0.5$	0	9.79×10^{-4}	9.79×10^{-4}	9.29×10^{-4}	9.29×10^{-4}
	0.0540	9.67×10^{-4}	9.78×10^{-5}	4.91×10^{-5}	1.37×10^{-6}
	0.111	1.22×10^{-3}	2.79×10^{-5}	5.29×10^{-5}	5.17×10^{-6}
	0.171	1.15×10^{-3}	2.42×10^{-5}	2.78×10^{-5}	8.45×10^{-5}
	0.236	1.25×10^{-3}	9.10×10^{-6}	1.12×10^{-4}	2.76×10^{-5}
$Z = 1.5$	0	9.48×10^{-4}	9.54×10^{-4}	3.41×10^{-7}	3.41×10^{-7}
	0.0540	1.02×10^{-3}	2.87×10^{-4}	5.89×10^{-7}	3.97×10^{-8}
	0.111	1.16×10^{-3}	1.80×10^{-4}	1.45×10^{-8}	2.35×10^{-4}
	0.171	1.25×10^{-3}	1.35×10^{-4}	2.70×10^{-6}	1.06×10^{-4}
	0.236	1.33×10^{-3}	4.77×10^{-5}	3.14×10^{-7}	4.87×10^{-5}
$Z = 3.0$	0	1.38×10^{-3}	1.38×10^{-3}	8.55×10^{-12}	8.55×10^{-12}
	0.0540	1.54×10^{-3}	4.34×10^{-4}	3.46×10^{-9}	2.61×10^{-5}
	0.111	1.81×10^{-3}	2.89×10^{-4}	5.02×10^{-10}	5.43×10^{-7}
	0.171	2.13×10^{-3}	2.35×10^{-4}	4.82×10^{-8}	2.50×10^{-5}
	0.236	2.54×10^{-3}	2.13×10^{-4}	5.07×10^{-9}	1.59×10^{-5}

Table 1: Relative error for approximating the value of $\log \det(\mathbf{V}(ik)\tilde{\mathbf{V}}(ik)^{-1})$ on the first five consecutive quadrature points via the inverse-free Krylov subspace and standard Arnoldi methods with/without subspace recycled. The scatterers are two spheres with equal radii $R = 1$ with distance $Z = 0.5, 1.5$ and 3.0 . The sphere meshes are refined with size $h = 0.1$.

For large problems the dominating cost is that of the involved matrix-vector products with the integral operators. [In Figures 4 and 5 we plot the number of actual matvecs with the discretised matrix form \$\mathbf{V}\(ik\)\$ for each individual algorithm](#). The integral here has been discretized with 20 quadrature points. [What is the number of quad points? You need to give this information. Do you count the matvec with each component of the 2x2 block matrices \$V_{ik}\$ and \$\tilde{V}_{ik}\$ separately? Not clear from your description.](#)

It shows that the recycling strategy significantly reduces the overall number of matrix-vector products necessary.

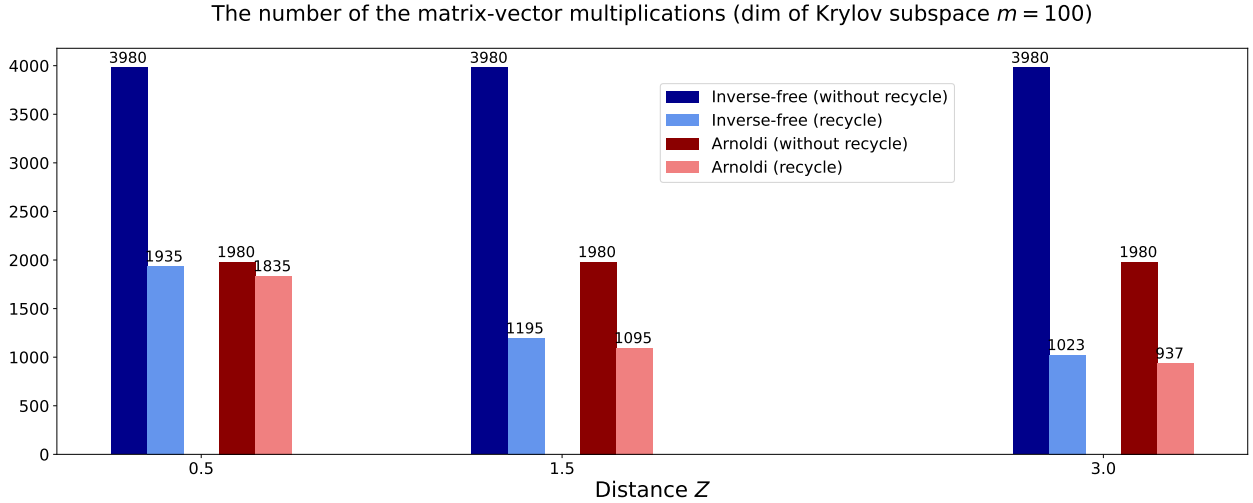


Figure 4: The number of the matrix-vector products inside inverse-free and standard Arnoldi methods with or without recycling subspace. The scatterers are two spheres with equal radii $R = 1$ and distance Z is 0.5, 1.5 and 3.0. The dimension of the Krylov subspace is set as $m = 100$.

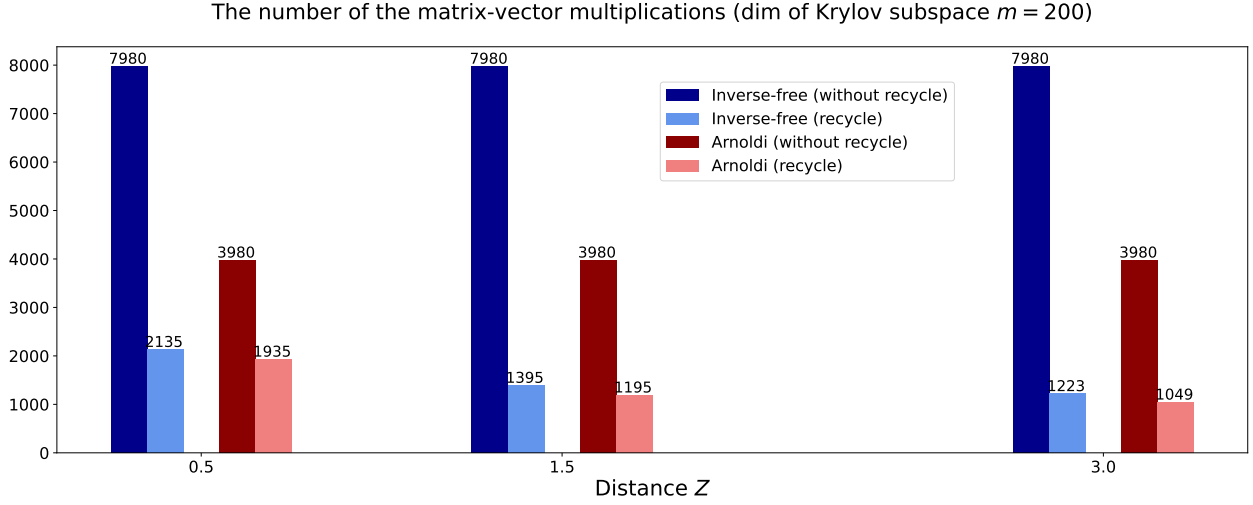


Figure 5: The number of the matrix-vector products inside inverse-free and standard Arnoldi methods with or without recycling subspace. The scatterers are two spheres with equal radii $R = 1$ and distance Z is 0.5, 1.5 and 3.0. The dimension of the Krylov subspace is set as $m = 200$.

4. Numerical experiments

In this section, we demonstrate numerical results for computing the Casimir energy between two conducting objects, where the objects are spheres, Menger sponges, ice crystals and ellipsoids. Reference values for the Casimir energy in each case is computed by grid refinement plus Richardson extrapolation.

In the case of spheres we also compare with known asymptotic expansions [24].

4.1. Two spheres case

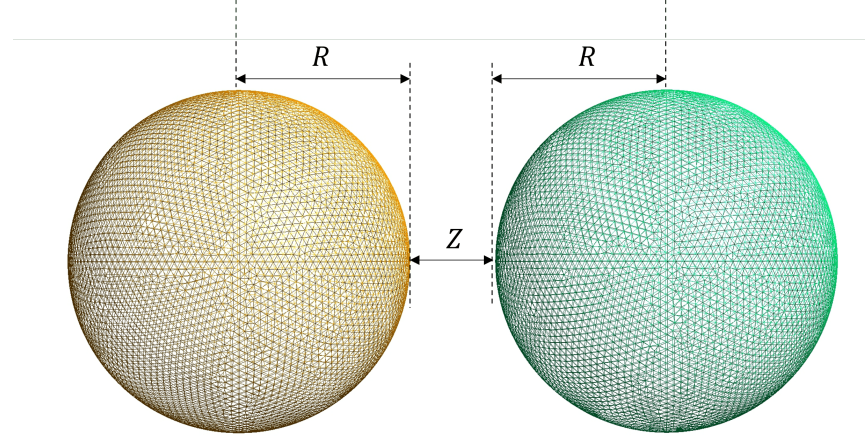


Figure 6: Two spheres with equal radii: $R = 1$ represents the radius of the spheres and Z is the distance between them. $h_{\text{coarse}} = 0.1$: $\dim(V_{ik}) = 3192$, N^{Ω} of elements on both grids = 6384; $h_{\text{fine}} = 0.05$: $\dim(V_{ik}) = 12603$, N^{Ω} of elements on both grids = 25180

We start with validating the construction of the integrand function Ξ of the Casimir integral (5) in the case when the scatterers are two perfectly conducting spheres with equal radii R and distance Z (see Figure 6). Denote by Ξ_h the value of Ξ computed under the refinement level with mesh size h and denote by $\Xi_{\text{ref}}(ik)$ the reference values computed by discretizing the single-layer boundary integral operators in terms of the spherical harmonic functions, which is suggested by [26]. These reference values are accurate within 0.05%.

Figure 7 shows the relative distance between $\Xi_h(ik)$ and $\Xi_{\text{ref}}(ik)$ in difference refinement levels with $ik = 0.8i$. One can see that Ξ_h converges to Ξ_{ref} with the mesh refined. This figure is plotted in log-log scale plot and the slope of these lines is around 2. This numerical result indicates that this convergence is quadratic.

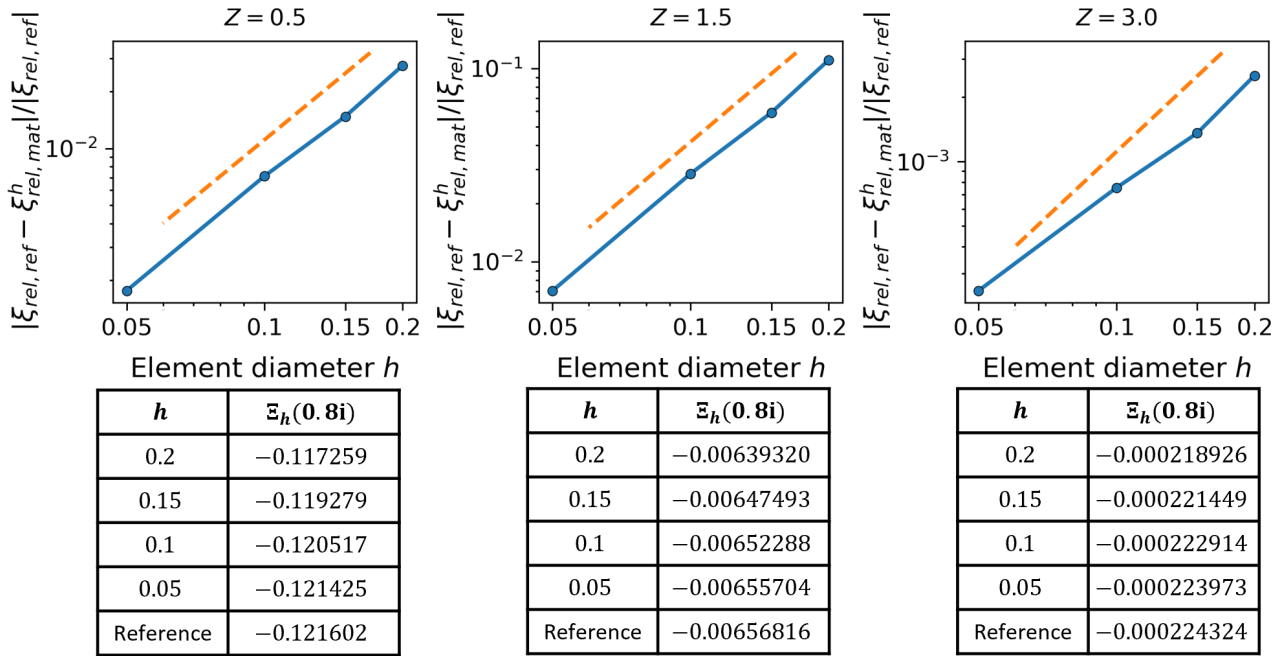


Figure 7: h -convergence of $\Xi_h(ik)$ when $ik = 0.8i$. The reference value Ξ_{ref} is accurate within 0.05%. The scatterers are two spheres with equal radii 1 and the distance between them is set as $Z = 0.5, 1.5$ and 3.0 . The relative distance between Ξ_{ref} and Ξ_h decreases as we refine the mesh.

Having shown the validation of the construction of Ξ , we are left with determining a proper upperbound for the Casimir integration. The following asymptotic expression of the integrand of the Casimir integral formula

(5) introduced in [32] can help with determining the upperbound, which is written as:

$$\Xi(k) = -\frac{R_1 R_2}{4Z(R_1 + R_2 + Z)} e^{2iZk} + o(e^{-2Z\text{Im}k}), \quad (11)$$

where R_1 and R_2 are the radius of the spheres. I do not understand why you now use this expansion and in the earlier sentence cite [24]. Is this the same expansion? No, they are not the same expansion. [32] is from Alex's result about the asymptotic expression of the integrand and I used it for determine the upperbound of the integration. [24] is the asymptotic expansion of the Casimir energy

As I have said when we discussed your thesis. It is terrible to start with this Figure. People want to see some kind of validation of your results. But you compare with something that has quite different values.

Figure 8 plots the quotient of the leading term in (11) and the estimated integrand value on different wavenumbers ik . This quotient provides with a good estimate on the upperbound of the integration of the Casimir energy formula (5). For example, when the distance $Z = 1.5$, if k in wavenumber ik is larger than 7, the quotient gets far away from 1, which means the approximated integrand value is not close to the asymptotic term and $7i$ is chosen as the upperbound when $Z = 1.5$. The following table lists the upperbound of the integration for the distance Z varying from 0.5 to 3.0.

Distance Z	0.5	0.75	1.0	1.25	1.5	1.75	2.0	2.25	2.5	2.75	3.0
Upperbound	24i	17i	13i	9i	7i	6i	6i	5i	5i	4i	4i

Table 2: The estimated upperbound for the Casimir energy formula for different minimal distance Z varying from 0.5 to 3.0.

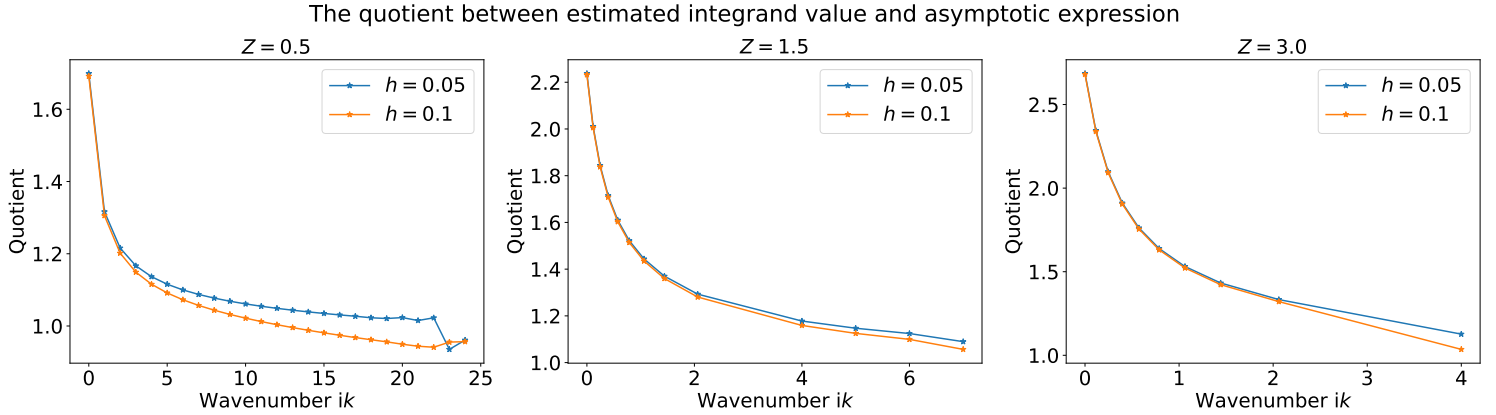


Figure 8: The quotient of the leading term of the series (11) and the estimated integrand value along the imaginary axis with grid size h set as $h_{\text{coarse}} = 0.1$ and $h_{\text{fine}} = 0.05$ in two spheres with equal radii's case. The radius of the spheres is $R = 1$ and the minimal distance between them is $Z = 0.5, 1.5$ and 3.0 .

Remark 2 (Determine the upperbound of the integration from the error tolerance). By Figure 1, since the integrand value $\log \det V_{ik} \tilde{V}_{ik}^{-1}$ shares the same trend with e^{-2Zk} in (5), one can apply the function $f(k) = Ce^{-2Zk}$ to fit the curve of the estimated integrand values. With the coefficient C determined, one can estimate the absolute error for approximating the Casimir integral by computing:

$$\epsilon \approx \int_{\kappa}^{\infty} f(k) dk = \frac{Ce^{-2Z\kappa}}{2Z},$$

where κ is the upperbound of the integration. Recall that we have changed the variable from k to $y = e^{-k}$ when applying the normal trapezoidal rule. This upperbound κ corresponds to the lowerbound of y , i.e. $e^{-\kappa}$.

You earlier do a coordinate transformation. So this upper bound turns into a lower bound for your quadrature rule. You should remark on this.

Meanwhile, one can also determine the upperbound of the integration with regard to different error tolerance.

For example, if one aims to have at least three significant digits of the exact value of the Casimir integral, the upperbound can be set as the following table lists:

Distance Z	0.5	0.75	1.0	1.25	1.5	1.75	2.0	2.25	2.5	2.75	3.0
Upperbound	10i	7i	5i	5i	4i	3i	3i	2i	2i	2i	2i

Table 3: The estimated upperbound for the Casimir energy formula for different minimal distance Z varying from 0.5 to 3.0.

With the upperbound of the integration determined, one can start to estimate the Casimir energy between two spheres with radius $R = 1$ at the distance of Z via the formula (5) in two different refinement levels: $h_{\text{fine}} = 0.05$ ($\dim(V_{ik}) = 12603$) and $h_{\text{coarse}} = 0.1$ ($\dim(V_{ik}) = 3192$).

Afterwards, the extrapolation result can be computed by these Casimir energy estimates. This result would be regarded as the extrapolation value of the Casimir energy, which would be used to compare with the estimates derived from the asymptotic series introduced below.

According to [24], the Casimir energy between two spheres (with equal radii R) at asymptotically large separations can be obtained as a series in terms of the ratio of centre distance L ($L = 2R + Z$) to sphere radius R :

$$\mathcal{E} = -\frac{\hbar c}{\pi} \frac{1}{L} \sum_{n=0}^{\infty} b_n \left(\frac{R}{L} \right)^{n+2}, \quad (12)$$

where the first six coefficients are $b_0 = -1/4$, $b_1 = -1/4$, $b_2 = -77/48$, $b_3 = -25/16$, $b_4 = -29837/2880$, $b_5 = -6491/1152$. Figure 9 shows the comparison between the Casimir energy computed from asymptotic series (12) and the exact value evaluated through Richardson extrapolation. Here, we observe that the asymptotic value gradually approaches to the exact value as the distance Z increases since the asymptotic expansion (12) only works when the distance between two spheres is asymptotically large.

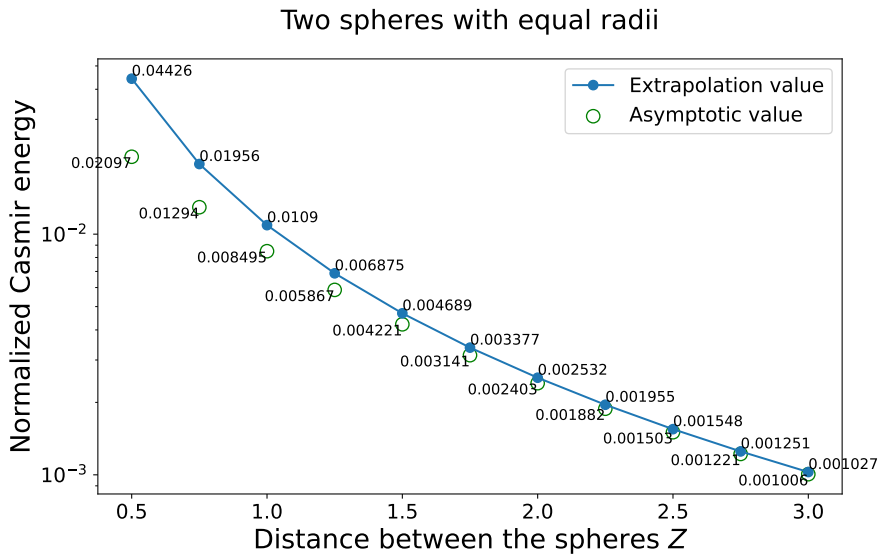


Figure 9: Normalized Casimir energy ²in two spheres with equal radii's case. The radius is $R = 1$ and the distance Z ranges from 0.5 to 3.0. The exact value of the (normalized) Casimir energy has been written beside the data point, which is round up to 4 significant digits.

²The normalized Casimir energy is $\mathcal{E}/\hbar c$, for \mathcal{E} defined in (5).

Figure 10 shows the relative distance between the estimated Casimir energy computed through inverse-free Krylov subspace method with subspace recycled (solid blue triangles), standard Arnoldi method with subspace recycled (solid red circles), asymptotic series (solid black squares) and the extrapolation values. For both efficient methods introduced in Section 3, the dimension of the Krylov subspace is set as $m = 100$. In addition, in the recycling process, only the eigenvectors associated with the extreme eigenvalues whose logarithm is larger than 10^{-s} , where $s = 3, 4, 5$ when $Z = 0.5 \sim 1.25, 1.5 \sim 2.75, 3.0$, respectively, would be extracted and recycled. With these settings, these two methods with subspace recycled can achieve at least three significant digits accuracy on approximating the Casimir energy.

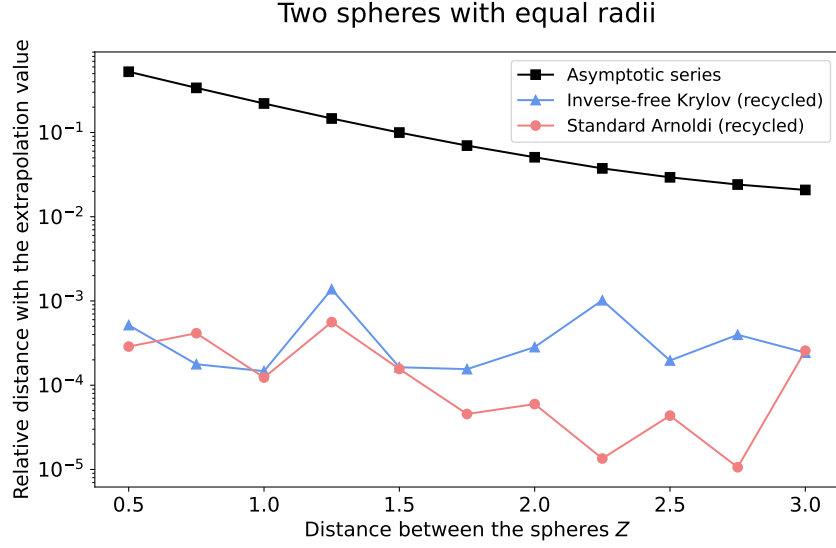


Figure 10: Spheres with equal radii's case: relative distance between the reference value (computed by Richardson extrapolation) with the asymptotic series (solid black square) and the estimates evaluated from the standard Arnoldi method with subspace recycled (solid red circles) and inverse-free Krylov subspace method with subspace recycled (solid blue triangles). The dimension of the Krylov subspace is $m = 100$. The recycled eigenvector has the corresponding eigenvalue whose logarithm is larger than 10^{-s} , where $s = 3, 4, 5$ when $Z = 0.5 \sim 1.25, 1.5 \sim 2.75, 3.0$, respectively.

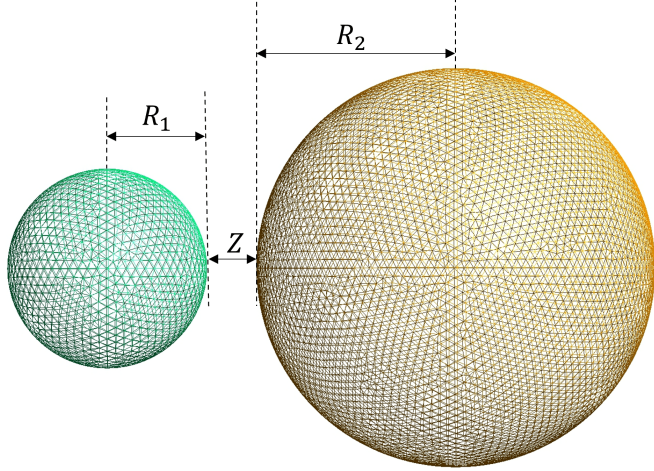


Figure 11: Two spheres with unequal radii: $R_1 = 0.5$ and $R_2 = 1$ represent the radius of the spheres and Z is the distance between them. $h_{\text{coarse}} = 0.1$: $\dim(V_{ik}) = 2023$, N^{Ω} of elements on both grids = 4038; $h_{\text{fine}} = 0.05$: $\dim(V_{ik}) = 7891$, N^{Ω} of elements on both grids = 15774

When the perfectly conducting spheres have different radii R_1, R_2 (see Figure 11), one can still use the asymptotic expansion (11) to determine the upperbound of the integration in the Casimir energy formula.

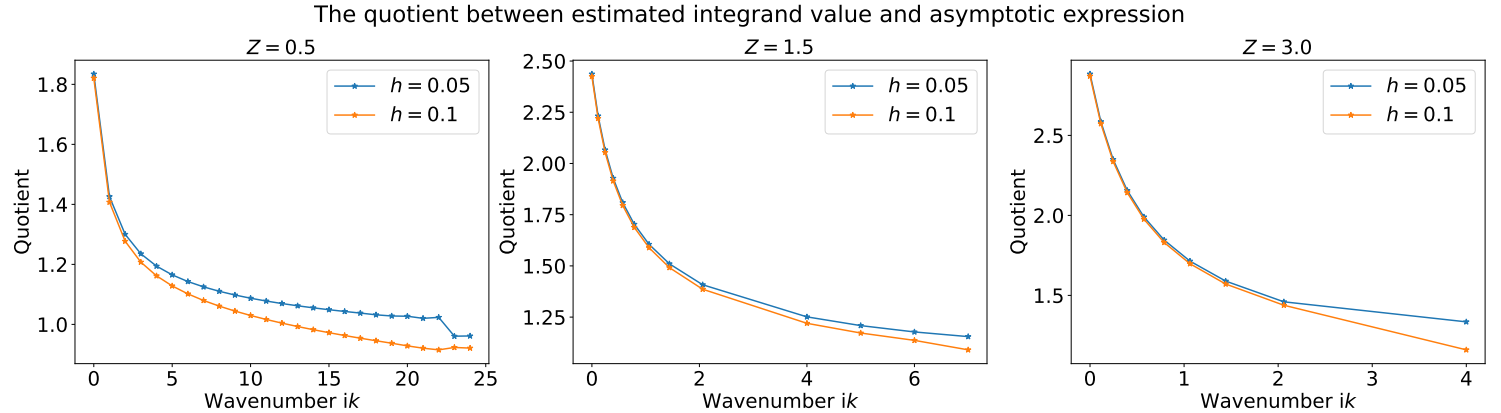


Figure 12: Absolute distance between the approximated integrand value of the Casimir energy formula and the first term in asymptotic expansion (11), and compare this value with the exponential $e^{-2Z\text{Im}k}$. The radii of the spheres are equal to $R_1 = 1$ and $R_2 = 0.5$, and the minimal distance Z between them is 0.5, 1.5 and 3.0. The absolute distance is in solid blue triangles when grid size $h = 0.1$ and in solid orange circles when $h = 0.05$.

Again, with Figure 12, one can easily estimate the upperbound and the results are listed in Table 4.

Distance Z	0.5	0.75	1.0	1.25	1.5	1.75	2.0	2.25	2.5	2.75	3.0
Upperbound	24i	17i	13i	9i	7i	6i	6i	5i	5i	4i	4i

Table 4: The estimated upperbound for the Casimir energy formula for different minimal distance Z varying from 0.5 to 3.0.

By recalling the Remark 2, in order to have at least three significant digits matching with the exact value of the Casimir energy, the upperbound can be set as:

Distance Z	0.5	0.75	1.0	1.25	1.5	1.75	2.0	2.25	2.5	2.75	3.0
Upperbound	10i	6i	6i	4i	4i	3i	3i	3i	3i	3i	3i

Table 5: The estimated upperbound for the Casimir energy formula for different minimal distance Z varying from 0.5 to 3.0.

Afterwards, by denoting the centre distance as $L = R_1 + R_2 + Z$, the asymptotic expansion of the Casimir energy at asymptotically large distance can be written as:

$$\mathcal{E} = -\frac{\hbar c}{\pi} \frac{1}{L} \sum_{n=0}^{\infty} \tilde{b}_n(\eta) \left(\frac{R_1}{L} \right)^{n+2}, \quad (13)$$

where the coefficients $\{\tilde{b}_n\}$ depend on the parameter $\eta = R_2/R_1$ and the first six coefficients are

$$\begin{aligned} \tilde{b}_0 &= -\frac{\eta}{4}, & \tilde{b}_1 &= -\frac{\eta + \eta^2}{8}, & \tilde{b}_2 &= -\frac{34(\eta + \eta^3) + 9\eta^2}{48}, & \tilde{b}_3 &= -\frac{2(\eta + \eta^4) + 23(\eta^2 + \eta^3)}{32}, \\ \tilde{b}_4 &= -\frac{8352(\eta + \eta^5) + 1995(\eta^2 + \eta^4) + 38980\eta^3}{5760}, & \tilde{b}_5 &= -\frac{-1344(\eta + \eta^6) + 5478(\eta^2 + \eta^5) + 2357(\eta^3 + \eta^4)}{2304}. \end{aligned}$$

In the following experiment, the radii of the spheres shown in Figure 11 are set as $R_1 = 0.5$ and $R_2 = 1$. As in the previous example, the exact value of the Casimir energy is computed through the Richardson extrapolation and the coarse and fine grid size are $h_{\text{fine}} = 0.05$ ($\dim(V_{ik}) = 7893$) and $h_{\text{coarse}} = 0.1$ ($\dim(V_{ik}) = 2023$), separately.

In this case, the asymptotic value of the Casimir energy was estimated by the series (13) and the comparison between the exact value and asymptotic one is shown in Figure 13. Again, one can notice that when the distance between two spheres decreases, the asymptotic value gets close to the exact one and the reason for this is clearly stated in the above equal radii's case.

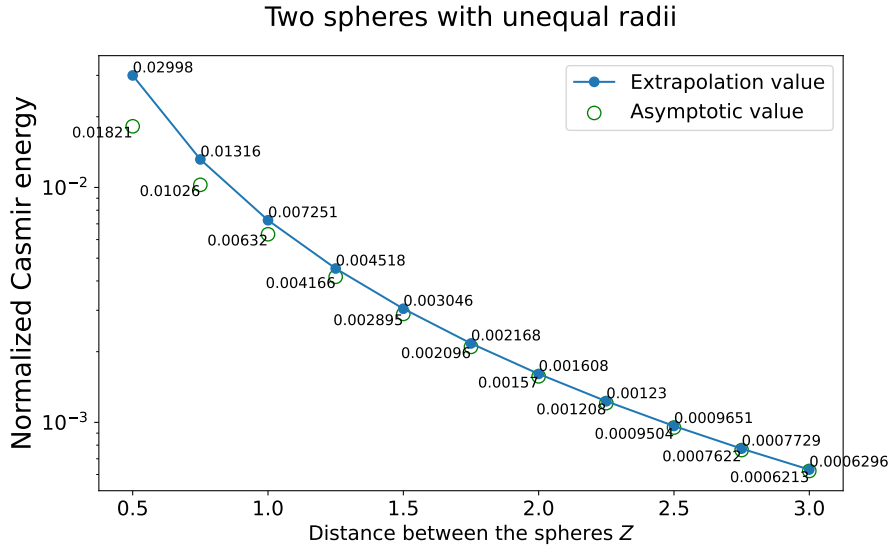


Figure 13: Normalized Casimir energy in two spheres with unequal radii's case. The radius is $R = 1$ and the distance Z ranges from 0.5 to 3.0. The exact value of the (normalized) Casimir energy has been written beside the data point, which is round up to 4 significant digits.

By keeping all the experimental settings being the same with the equal radii's case, the numerical experiments on testing the performance of the inverse-free and standard Arnoldi methods with subspace recycled have been done in the unequal radii's case and the results are shown in Figure 14.

Two spheres with unequal radii

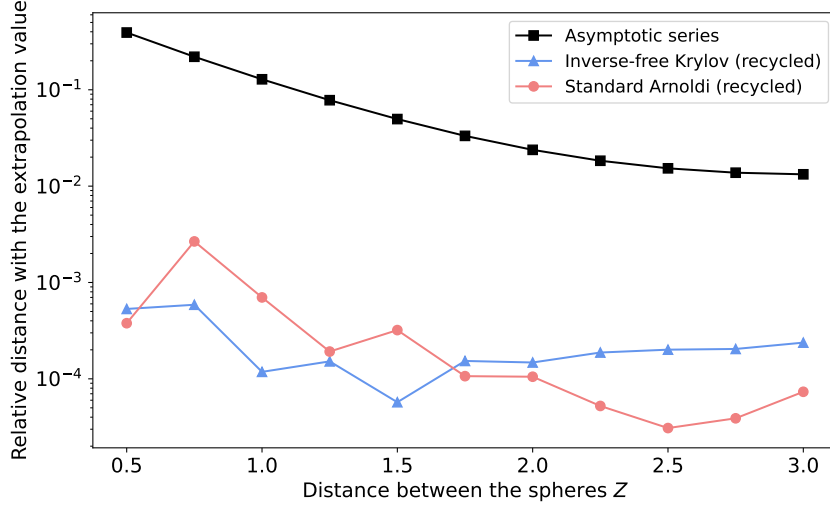


Figure 14: Spheres with unequal radii's case: relative distance between the reference value (computed by Richardson extrapolation) with the asymptotic series (solid black square) and the estimates evaluated from the standard Arnoldi method with subspace recycled (solid red circles) and inverse-free Krylov subspace method with subspace recycled (solid blue triangles). The dimension of the Krylov subspace is $m = 100$. The recycled eigenvector has the corresponding eigenvalue whose logarithm is larger than 10^{-s} , where $s = 3, 4, 5$ when $Z = 0.5 \sim 1.25, 1.5 \sim 2.75, 3.0$, respectively.

4.2. Realistic objects case

In this part, the Casimir energy between the objects with special shapes such as the menger sponges, ice crystals and ellipsoids will be computed through the Richardson extrapolation mentioned in the beginning of this section and the values labelled in the following figures are always round up to 4 significant digits.

Figure 15 plots the menger sponges in different levels (0, 1 and 2) and the length of these sponges is always 1. Afterwards, the Casimir energy between two menger sponges in the same level are listed in Table 6. In addition, inside the extrapolation process, when $h_{\text{fine}} = 0.05$, the $\dim(V_{ik}) = 5664, 8510$ and 27136 and when $h_{\text{coarse}} = 0.1$, the $\dim(V_{ik}) = 1456, 3092$ and 14464 in different level (0, 1 and 2) cases, separately. By comparing the data point in this table, it is easy to find that the Casimir energy decreases as the number of the iteration increases since the cross-sectional area gets smaller.

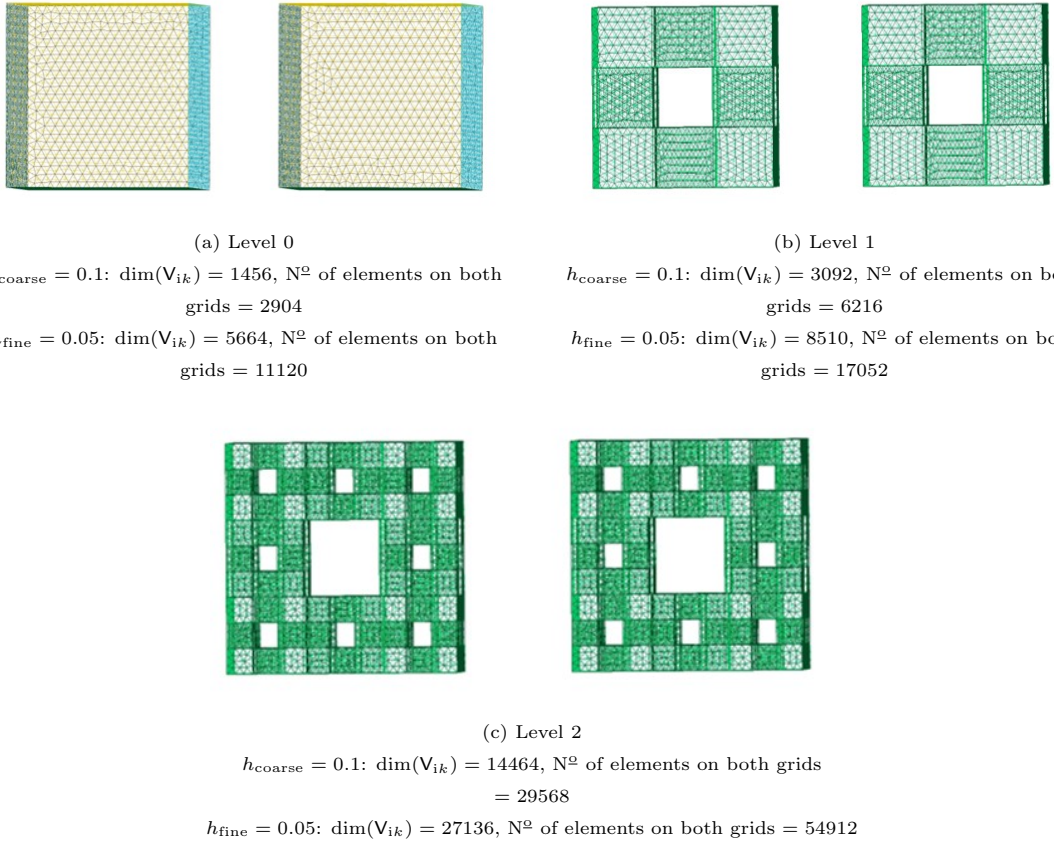


Figure 15: Menger sponges in different levels. The length of each sponge is 1.

Normalized Casimir energy in two menger sponges' case			
Distance	Level 0	Level 1	Level 2
0.5	0.08350	0.08229	0.08112
0.75	0.02737	0.02688	0.02670
1.0	0.01305	0.01288	0.01282
1.25	0.007357	0.007283	0.007252
1.5	0.004607	0.004568	0.004551
1.75	0.003099	0.003076	0.003065
2.0	0.002195	0.002181	0.002174
2.25	0.001618	0.001608	0.001603
2.5	0.001230	0.001223	0.001220
2.75	0.0009593	0.0009541	0.0009514
3.0	0.0007638	0.0007598	0.0007577

Table 6: Normalized Casimir energy in two menger sponges' case

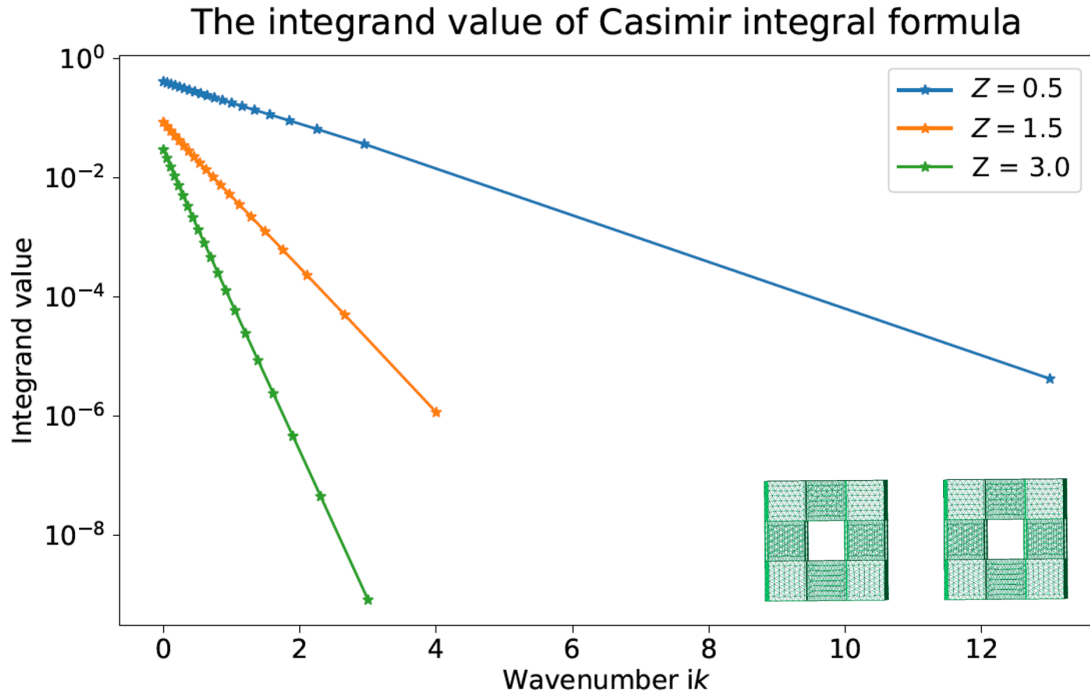


Figure 16: The integrand of the Casimir energy between two menger sponges in Level 1 with distance $Z = 0.5, 1.5$ and 3.0 .

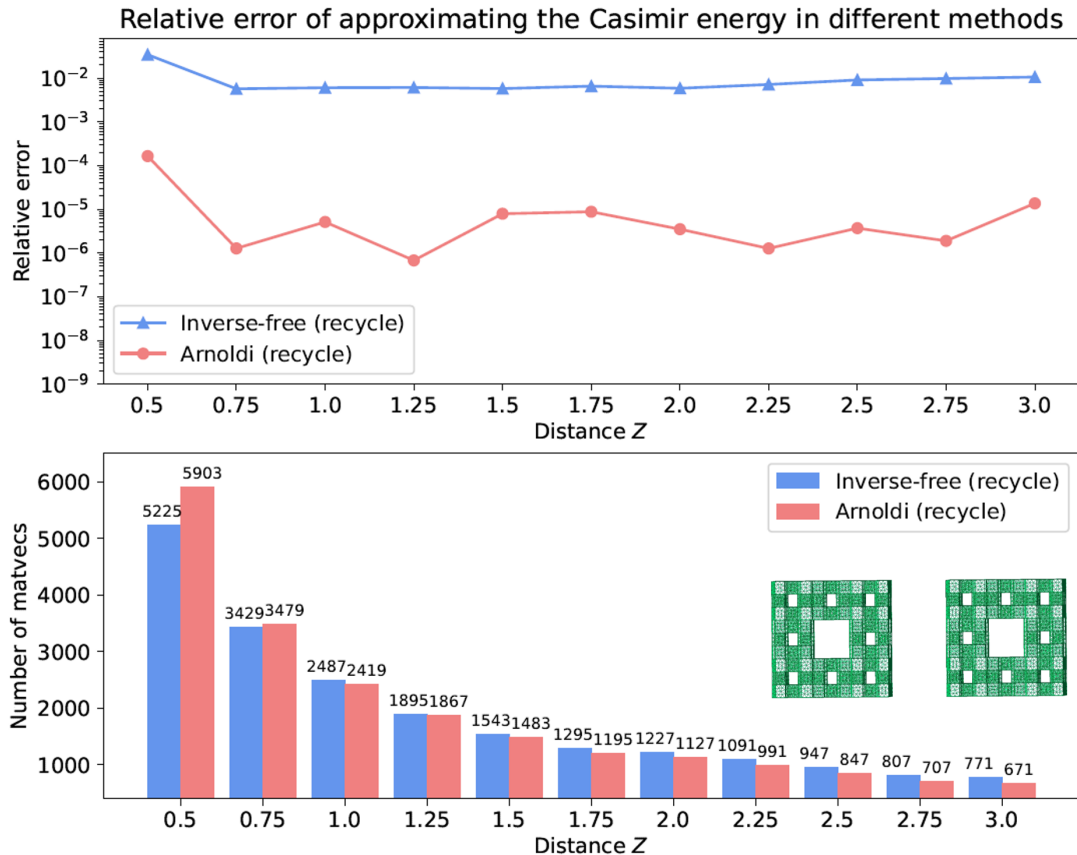
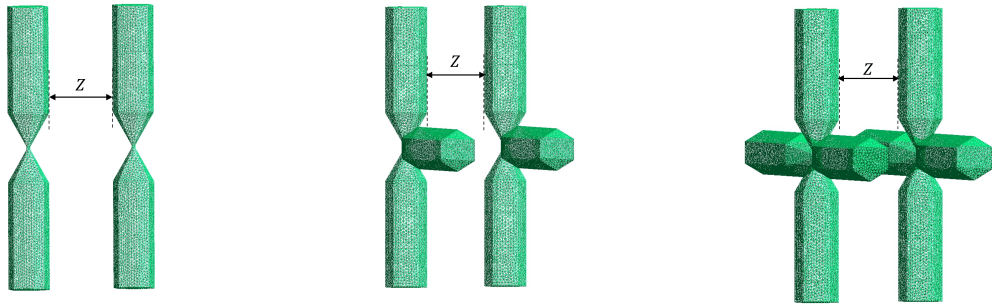


Figure 17: Menger sponges in Level 2's case: relative distance between the reference value (computed by Richardson extrapolation) with the estimates evaluated from the standard Arnoldi method with subspace recycled (solid red circles) and inverse-free Krylov subspace method with subspace recycled (solid blue triangles). The dimension of the Krylov subspace is $m = 100$. The recycled eigenvector has the corresponding eigenvalue whose logarithm is larger than 10^{-5} .

In the next example, the scatterers are ice crystals with different number of branches ranging from 2 to 6 (see Figure 18).



(a) Two branches: $\dim(V_{ik}) = 8792$
 N^o of elements on both grids = 17576

(b) Three branches: $\dim(V_{ik}) = 13104$
 N^o of elements on both grids = 26200

(c) Four branches: $\dim(V_{ik}) = 17554$
 N^o of elements on both grids = 35100



(d) Five branches: $\dim(V_{ik}) = 21950$
 N^o of elements on both grids = 43900

(e) Six branches: $\dim(V_{ik}) = 26262$
 N^o of elements on both grids = 52556

Figure 18: Ice crystals with different number of branches

Normalized Casimir energy in ice crystals' case					
Distance	2-branches	3-branches	4-branches	5-branches	6-branches
0.5	0.04112	0.05989	0.07848	0.07873	0.01128
0.75	0.01499	0.02184	0.02855	0.02873	0.005017
1.0	0.007403	0.01080	0.01412	0.01428	0.002965
1.25	0.004242	0.006198	0.008113	0.008242	0.001985
1.5	0.002672	0.003905	0.005117	0.005223	0.001427
1.75	0.001797	0.002624	0.003442	0.003530	0.001074
2.0	0.001268	0.001849	0.002428	0.002501	0.0008357
2.25	0.0009288	0.001353	0.001776	0.001839	0.0006664
2.5	0.0007007	0.001019	0.001338	0.001391	0.0005410
2.75	0.0005413	0.0007863	0.001033	0.001078	0.0004469
3.0	0.0004270	0.0006188	0.0008134	0.0008526	0.0003741

Table 7: Normalized Casimir energy in 2- to 6-branched ice crystals' case

The integrand value of Casimir integral formula

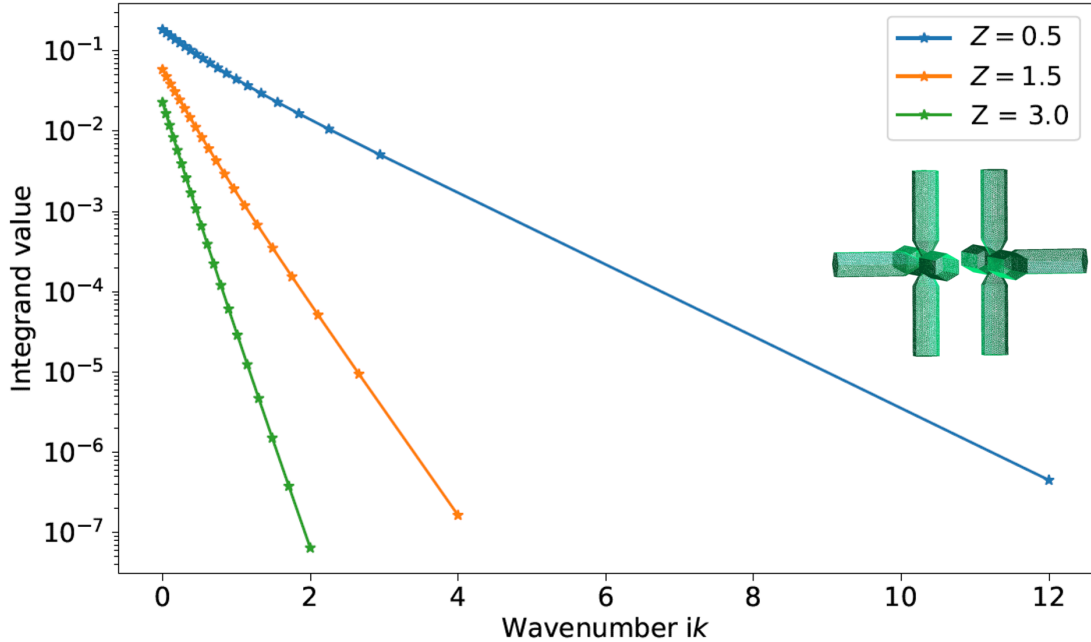


Figure 19: The integrand of the Casimir energy between two five-branches ice crystals with distance $Z = 0.5, 1.5$ and 3.0 .

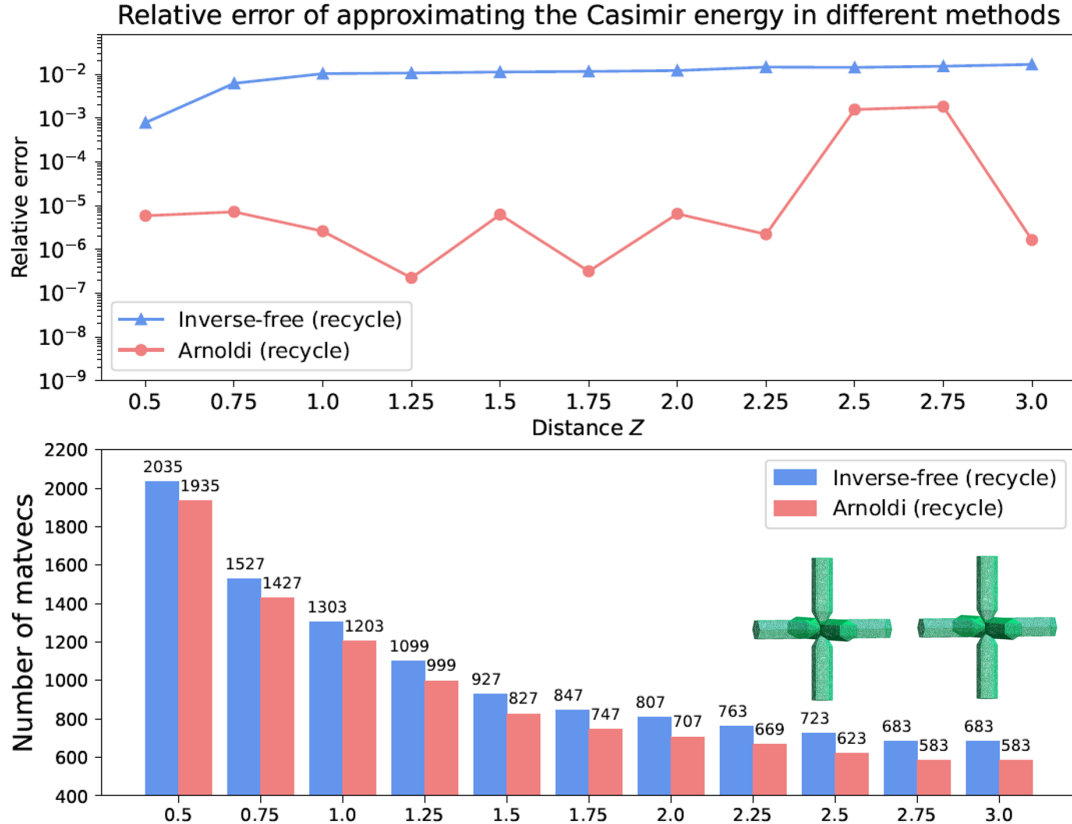


Figure 20: Six-branches ice crystals' case: relative distance between the reference value (computed by Richardson extrapolation) with the estimates evaluated from the standard Arnoldi method with subspace recycled (solid red circles) and inverse-free Krylov subspace method with subspace recycled (solid blue triangles). The dimension of the Krylov subspace is $m = 100$. The recycled eigenvector has the corresponding eigenvalue whose logarithm is larger than 10^{-5} .

For large problems, we can apply the fast multipole method (FMM)[42] when discretizing the operators. Compared with the dense assembly, it reduces the storage memory and also speed up the matrix assembly. Although it takes longer when multiplying the matrix assembled by FMM with the vectors, the

decreasing number of the matrix-vector products (see Figure 21 (Right)) leads to a shorter running time for computing the $\log \det(\mathbf{V}(ik)\tilde{\mathbf{V}}(ik)^{-1})$ (see Figure 21 (Left)).

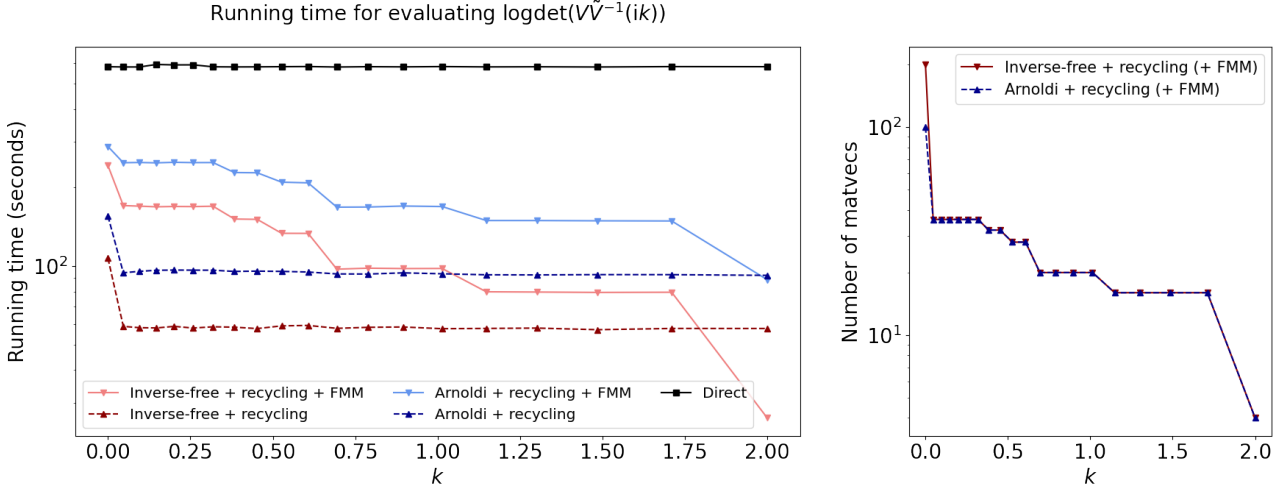
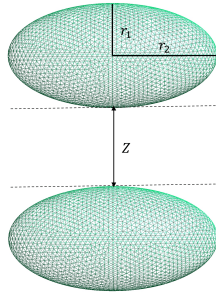


Figure 21: Six-branches ice crystals' case: (Left) running time for evaluating the $\log \det(\mathbf{V}(ik)\tilde{\mathbf{V}}(ik)^{-1})$ by the direct dense computation and the recycling approaches with/without implementing FMM. The expansion order for FMM is 7. (Right) The number of the matrix-vector products in the recycling approaches with/without implementing FMM for each wavenumber case.

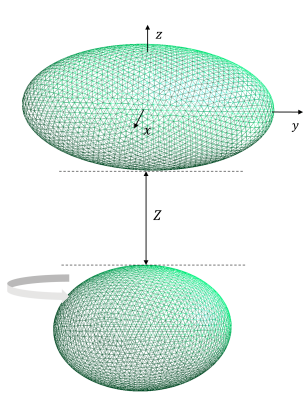
It is not hard to imagine that the Casimir energy would be different when rotating the scatterers and keeping the distance between them unchanged. Therefore, in the last example, we would see how the Casimir energy between two identical ellipsoids changes as one of the ellipsoids rotates.

In Figure 22a, the above ellipsoid is centering at $(0, 0, 0)$ and the below one is centering at $(0, 0, -(0.5 + 0.5 + Z))$, where Z is the distance between these two ellipsoids. Without rotation, the Casimir energy between them with different distance Z is plotted in Figure 23a.

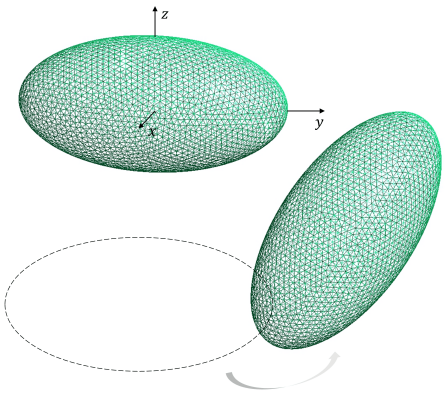
To explore how the rotation affects the change of the Casimir energy, one can always keep one ellipsoid fixed and rotate the other one. The Figure 22b and 22c describe the case when one of the ellipsoids rotates around z - and x -axis, respectively. From the Figure 23b, the Casimir energy changes periodically since we rotate one ellipsoid around z - or x -axis by 360 degrees.



(a) Without rotation



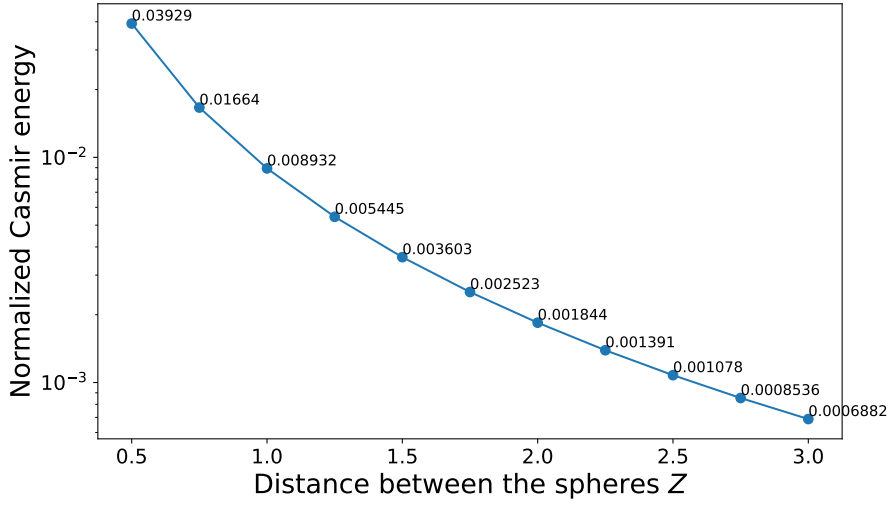
(b) Rotation around z-axis



(c) Rotation around x-axis

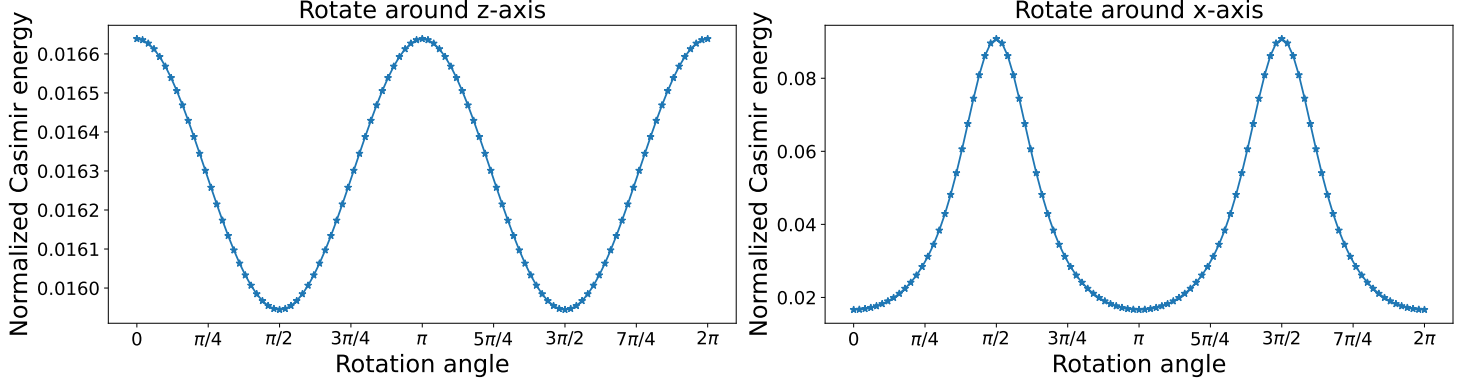
Figure 22: Two ellipsoids with or without rotation: when $h_{\text{fine}} = 0.05$, $\dim(\mathcal{V}_{ik}) = 5517$; $h_{\text{coarse}} = 0.1$, $\dim(\mathcal{V}_{ik}) = 1498$. The principal semi-axes of two ellipsoids are $r_1 = 0.5$ and $r_2 = 1.0$.

Casimir energy between two ellipsoids without rotations



(a) Casimir energy between two ellipsoids with different distances

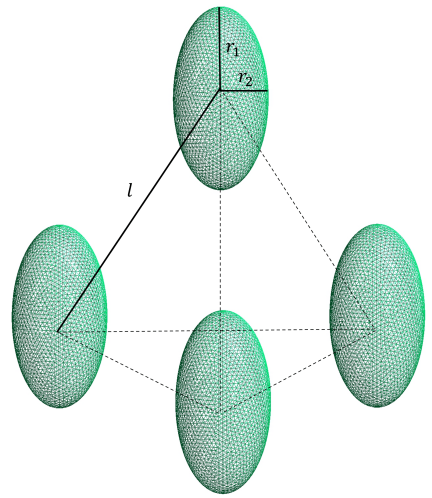
Casimir energy between two ellipsoids with rotations



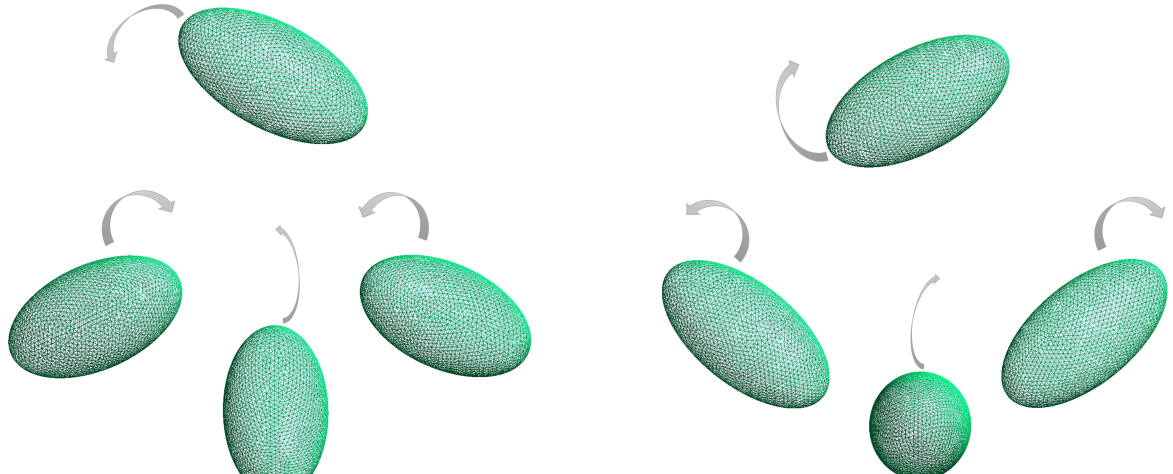
(b) Casimir energy when one of the ellipsoids rotates

Figure 23: The dependence of the Casimir energy and rotation angle of one of the ellipsoids.

Now, consider 4 ellipsoids located on the vertices of a regular tetrahedron with edge length $l = 2$ (Figure 24) and the principal semi-axes of all these ellipsoids are $r_1 = 0.6$ and $r_2 = 0.3$. Figure 24b and Figure 24c show the rotation of the ellipsoids inwards and outwards 360 degrees towards the centroid of this tetrahedron, separately. Afterwards, in order to use the Richardson extrapolation method to estimate the Casimir energy, we evaluate the integral (5) with the grid size set as $h_{\text{fine}} = 0.05$ and $h_{\text{coarse}} = 0.03$. Note that the number of the scatterers has increased to four, the matrices V_{ik} and \tilde{V}_{ik} have become to 4 by 4 block and diagonal block matrix, respectively. From the Figure 25, it shows that the Casimir energy between these four ellipsoids changes periodically with the rotation.



(a) No rotation



(b) Rotation inwards

(c) Rotation outwards

Figure 24: Four ellipsoids with or without rotations: when $h_{\text{fine}} = 0.03$, $\dim(V_{ik}) = 11024$; $h_{\text{coarse}} = 0.05$, $\dim(V_{ik}) = 4160$. The principal semi-axes of these ellipsoids are $r_1 = 0.6$ and $r_2 = 0.3$ and they locate on the vertices of a regular octahedron with edge length $l = 2$.

Casimir energy between four ellipsoids with rotations

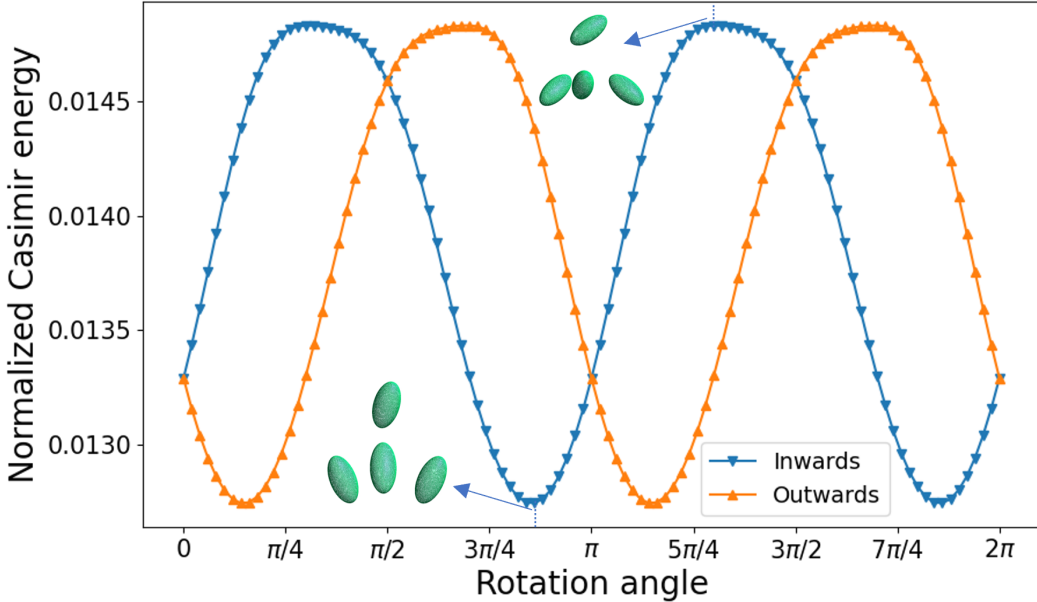


Figure 25: The dependence of the Casimir energy and rotation angle of one of the ellipsoids. Inwards towards the centroid case (solid blue square). Outwards towards the centroid case (solid orange triangle).

The scatterers of the last example are described inside the Figure 26. These six ellipsoids locate on the vertices of a regular octahedron with edge length $l = 2$ and again the principal semi-axes of all these ellipsoids are $r_1 = 0.6$ and $r_2 = 0.3$ (shown in the Figure 26). This time, the ellipsoids rotate inwards and outwards 360 degrees towards the centroid of this octahedron (Figure 26b and Figure 26c). By closely looking at these two rotation figures, we can notice that Figure 26b can be obtained by rotating Figure 26c 180 degrees. Therefore, the Casimir energies for the inwards and outwards cases are the same. Figure (27) shows how the Casimir energy changes among these six ellipsoids as they rotate.

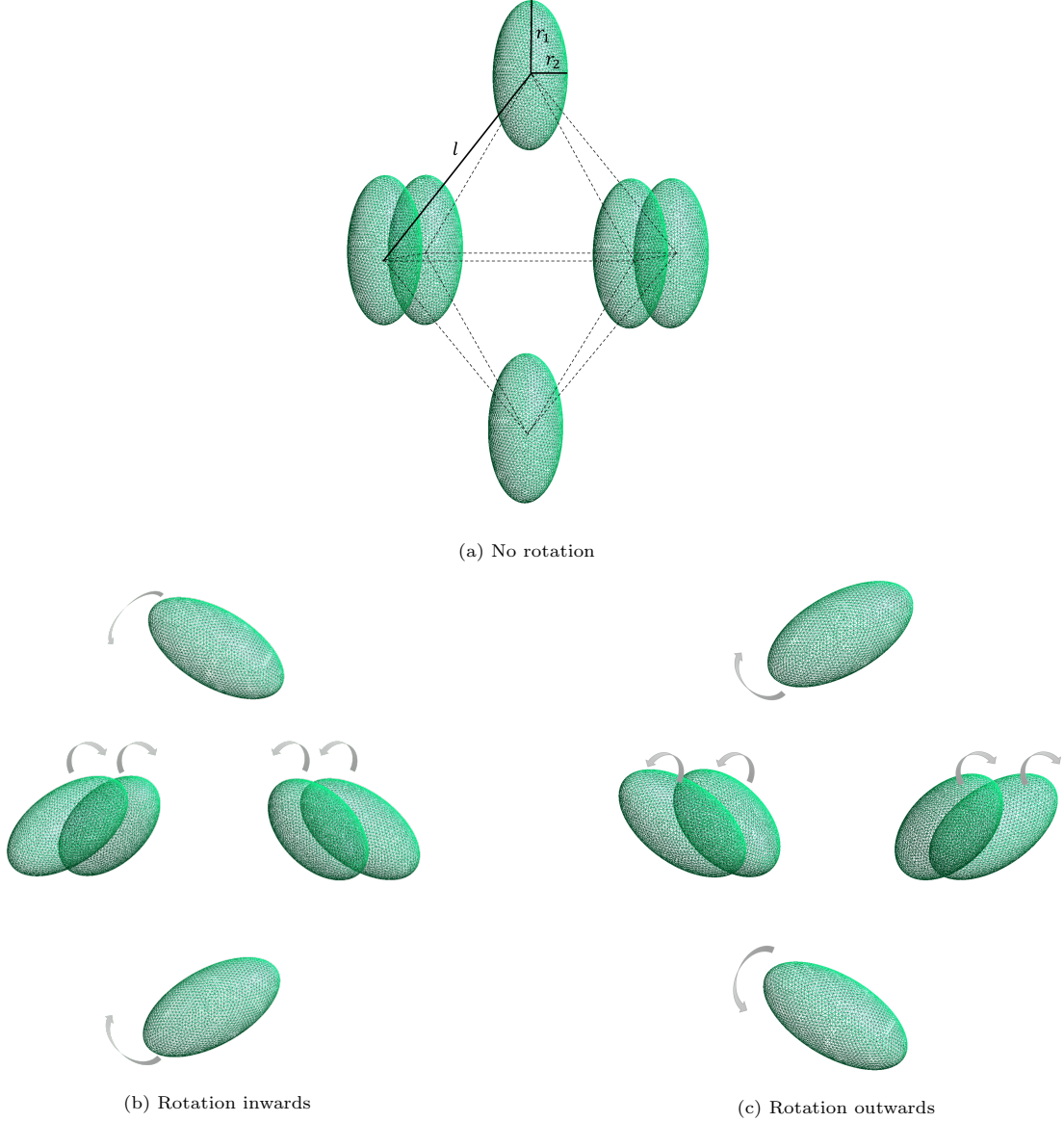


Figure 26: Six ellipsoids with or without rotations: when $h_{\text{fine}} = 0.03$, $\dim(V_{ik}) = 16536$; $h_{\text{coarse}} = 0.05$, $\dim(V_{ik}) = 6240$. The principal semi-axes of these ellipsoids are $r_1 = 0.6$ and $r_2 = 0.3$ and they locate on the vertices of a regular octahedron with edge length $l = 2$.

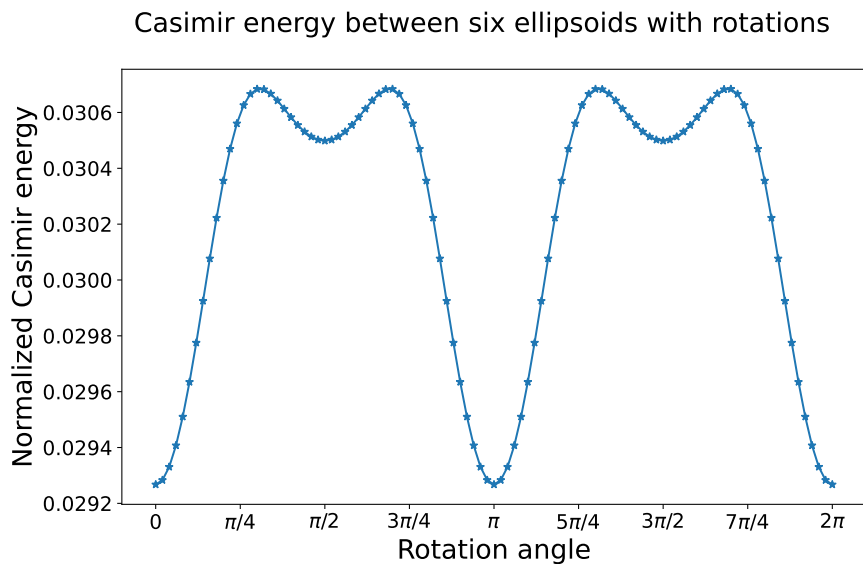


Figure 27: The dependence of the Casimir energy and rotation angle of one of the ellipsoids.

5. Conclusion

We have introduced the representation of the Casimir energy in terms of the boundary integral operators and its connection to the relative Krein spectral shift function. With the rigorous proof of the Casimir energy formula, we present several numerical methods for the calculation of the Casimir energy by applying the spectral properties of the Galerkin discretized form of the boundary integral operators. These methods are based on the classical Krylov subspace projection methods and subspaces recycled also significantly reduce the number of the matrix-vector multiplications and speed up the calculations for large-scale practical problems. For the future work, we will consider the calculation of the Casimir energy for the electromagnetic scattering case and implement the fast multipole method for larger practical problems.

References

- [1] H. B. Casimir, On the attraction between two perfectly conducting plates, in: Proc. Kon. Ned. Akad. Wet., Vol. 51, 1948, p. 793.
- [2] M. J. Sparnaay, Measurements of attractive forces between flat plates, *Physica* 24 (6-10) (1958) 751–764.
- [3] S. K. Lamoreaux, Demonstration of the casimir force in the 0.6 to $6 \mu\text{m}$ range, *Physical Review Letters* 78 (1) (1997) 5.
- [4] T. Ederth, Template-stripped gold surfaces with 0.4-nm rms roughness suitable for force measurements: Application to the casimir force in the 20–100-nm range, *Physical Review A* 62 (6) (2000) 062104.
- [5] G. Bressi, G. Carugno, R. Onofrio, G. Ruoso, Measurement of the casimir force between parallel metallic surfaces, *Physical review letters* 88 (4) (2002) 041804.
- [6] D. Krause, R. Decca, D. López, E. Fischbach, Experimental investigation of the casimir force beyond the proximity-force approximation, *Physical review letters* 98 (5) (2007) 050403.
- [7] H. B. Chan, Y. Bao, J. Zou, R. Cirelli, F. Klemens, W. Mansfield, C. Pai, Measurement of the casimir force between a gold sphere and a silicon surface with nanoscale trench arrays, *Physical review letters* 101 (3) (2008) 030401.
- [8] M. Bordag, U. Mohideen, V. M. Mostepanenko, New developments in the casimir effect, *Physics reports* 353 (1-3) (2001) 1–205.
- [9] M. Bordag, G. L. Klimchitskaya, U. Mohideen, V. M. Mostepanenko, *Advances in the Casimir effect*, Vol. 145, OUP Oxford, 2009.
- [10] E. Elizalde, A. Romeo, Expressions for the zeta-function regularized casimir energy, *Journal of mathematical physics* 30 (5) (1989) 1133–1139.
- [11] E. Elizalde, A. Romeo, Heat-kernel approach to the zeta-function regularization of the casimir energy for domains with curved boundaries, *International Journal of Modern Physics A* 5 (09) (1990) 1653–1669.
- [12] K. Kirsten, *Spectral functions in mathematics and physics*, Chapman and Hall/CRC, 2001.
- [13] I. E. Dzyaloshinskii, E. M. Lifshitz, L. P. Pitaevskii, The general theory of van der waals forces, *Advances in Physics* 10 (38) (1961) 165–209.

- [14] L. S. Brown, G. J. Maclay, Vacuum stress between conducting plates: an image solution, *Physical Review* 184 (5) (1969) 1272.
- [15] D. Deutsch, P. Candelas, Boundary effects in quantum field theory, *Physical Review D* 20 (12) (1979) 3063.
- [16] B. S. Kay, Casimir effect in quantum field theory, *Physical Review D* 20 (12) (1979) 3052.
- [17] G. Scharf, W. Wreszinski, On the casimir effect without cutoff, *Foundations of Physics Letters* 5 (5) (1992) 479–487.
- [18] S. A. Fulling, et al., Vacuum energy as spectral geometry, *SIGMA. Symmetry, Integrability and Geometry: Methods and Applications* 3 (2007) 094.
- [19] M. Renne, Microscopic theory of retarded van der waals forces between macroscopic dielectric bodies, *Physica* 56 (1) (1971) 125–137.
- [20] G. Bimonte, T. Emig, M. Kardar, M. Krüger, Nonequilibrium fluctuational quantum electrodynamics: Heat radiation, heat transfer, and force, *Annual Review of Condensed Matter Physics* 8 (2017) 119–143.
- [21] T. Emig, N. Graham, R. Jaffe, M. Kardar, Casimir forces between arbitrary compact objects, *Physical review letters* 99 (17) (2007) 170403.
- [22] T. Emig, R. Jaffe, M. Kardar, A. Scardicchio, Casimir interaction between a plate and a cylinder, *Physical review letters* 96 (8) (2006) 080403.
- [23] T. Emig, R. Jaffe, Casimir forces between arbitrary compact objects, *Journal of Physics A: Mathematical and Theoretical* 41 (16) (2008) 164001.
- [24] T. Emig, N. Graham, R. Jaffe, M. Kardar, Casimir forces between compact objects: The scalar case, *Physical Review D* 77 (2) (2008) 025005.
- [25] O. Kenneth, I. Klich, Opposites attract: A theorem about the casimir force, *Physical review letters* 97 (16) (2006) 160401.
- [26] O. Kenneth, I. Klich, Casimir forces in a t-operator approach, *Physical Review B* 78 (1) (2008) 014103.
- [27] K. A. Milton, J. Wagner, Multiple scattering methods in casimir calculations, *Journal of Physics A: Mathematical and Theoretical* 41 (15) (2008) 155402.
- [28] S. J. Rahi, T. Emig, N. Graham, R. L. Jaffe, M. Kardar, Scattering theory approach to electrodynamic casimir forces, *Physical Review D* 80 (8) (2009) 085021.
- [29] F. Hanisch, A. Strohmaier, A. Waters, A relative trace formula for obstacle scattering, arXiv preprint arXiv:2002.07291 (2020).
- [30] A. Strohmaier, The classical and quantum photon field for non-compact manifolds with boundary and in possibly inhomogeneous media, *Communications in Mathematical Physics* 387 (3) (2021) 1441–1489.
- [31] Y.-L. Fang, A. Strohmaier, A mathematical analysis of casimir interactions i: The scalar field, in: *Annales Henri Poincaré*, Springer, 2021, pp. 1–51.
- [32] Y.-L. Fang, A. Strohmaier, Singularity traces in obstacle scattering and the poisson relation for the relative trace, arXiv preprint arXiv:2104.01017 (2021).

- [33] M. W. Scroggs, T. Betcke, E. Burman, W. Šmigaj, E. van't Wout, Software frameworks for integral equations in electromagnetic scattering based on calderón identities, *Computers & Mathematics with Applications* 74 (11) (2017) 2897–2914.
- [34] P. Waterman, New formulation of acoustic scattering, *The journal of the acoustical society of America* 45 (6) (1969) 1417–1429.
- [35] M. Ganesh, S. C. Hawkins, A far field based t-matrix method for three dimensional acoustic scattering, *ANZIAM Journal* 50 (2008) 121–136.
- [36] Y.-L. Fang, A. Strohmaier, Trace singularities in obstacle scattering and the poisson relation for the relative trace, *Annales mathématiques du Québec* 46 (1) (2022) 55–75.
- [37] R. Mathias, Quadratic residual bounds for the hermitian eigenvalue problem, *SIAM journal on matrix analysis and applications* 19 (2) (1998) 541–550.
- [38] G. H. Golub, Q. Ye, An inverse free preconditioned krylov subspace method for symmetric generalized eigenvalue problems, *SIAM Journal on Scientific Computing* 24 (1) (2002) 312–334.
- [39] J. H. Money, Q. Ye, Algorithm 845: Eigifp: A matlab program for solving large symmetric generalized eigenvalue problems, *ACM Transactions on Mathematical Software (TOMS)* 31 (2) (2005) 270–279.
- [40] W. E. Arnoldi, The principle of minimized iterations in the solution of the matrix eigenvalue problem, *Quarterly of applied mathematics* 9 (1) (1951) 17–29.
- [41] Y. Saad, Numerical methods for large eigenvalue problems: revised edition, SIAM, 2011.
- [42] L. Ying, G. Biros, D. Zorin, A kernel-independent adaptive fast multipole algorithm in two and three dimensions, *Journal of Computational Physics* 196 (2) (2004) 591–626.